

# Direct Evidence of Mechanical and Radiative Feedback from the Quasar in IRAS 09104+4109

K. W. Cavagnolo,<sup>1,2,3\*</sup> M. Donahue,<sup>3</sup> B. R. McNamara,<sup>1,4,5</sup> G. M. Voit,<sup>3</sup> and M. Sun,<sup>6</sup>

<sup>1</sup>University of Waterloo, Department of Physics and Astronomy, Waterloo, ON, Canada.

<sup>2</sup>UNS, CNRS UMR 6202 Cassiopée, Observatoire de la Côte d’Azur, Nice, France.

<sup>3</sup>Michigan State University, Department of Physics and Astronomy, East Lansing, MI, USA.

<sup>4</sup>Perimeter Institute for Theoretical Physics, Waterloo, ON, Canada.

<sup>5</sup>Harvard-Smithsonian Center for Astrophysics, Cambridge, MA, USA.

<sup>6</sup>University of Virginia, Department of Astronomy, Charlottesville, VA, USA.

Accepted (Year Month Day). Received (Year Month Day); in original form (Year Month Day)

## ABSTRACT

Using 77 ks of new data from the Chandra X-ray Observatory, we present a detailed study of the ultraluminous infrared brightest cluster galaxy (BCG) IRAS 09104+4109. Our X-ray analysis reveals the obscured active galactic nucleus (AGN) of IRAS 09104+4109 has previously excavated cavities in the host galaxy cluster intracluster medium (ICM) and is now beaming quasar-like radiation into the halo, photoionizing a galactic nebula and the ICM. From the cavity properties, we estimate the mechanical AGN power output at  $\approx 3 \times 10^{44} \text{ erg s}^{-1}$ , while the nuclear X-ray emission suggests a radiative AGN power output in excess of  $5 \times 10^{46} \text{ erg s}^{-1}$ , *i.e.* a radiative to mechanical ratio of  $\approx 200$ -to-1. In addition to the direct evidence of mechanical and radiative feedback impacting the extended IRAS 09104+4109 halo, we argue that the galaxy’s relative **dust-richness and gas poorness** indicate significant galactic-scale radiative feedback. From these results, we suggest that IRAS 09104+4109 clearly demonstrates the typical characteristics of systems experiencing “quasar-mode” and “radio-mode” feedback, implying that IRAS 09104+4109 is a rare transition object. Using the misalignment between the beamed nuclear radiation and the large-scale jets as a constraint, we explore a range of possible explanations for the nature of IRAS 09104+4109, such as a brief period of supercritical accretion and associated evolution of the supermassive black hole spin state. We go on to suggest that IRAS 09104+4109 may be a local example of how massive, high-redshift galaxies transition (or cycle) from a radiatively-dominated to a mechanically-dominated form of feedback.

**Key words:** cooling flows – galaxies: clusters: galaxies: individual (IRAS 09104+4109); clusters: individual (RX J0913.7+4056)

## 1 INTRODUCTION

The discovery of tight correlations between galaxy stellar bulge properties and the mass of their centrally located supermassive black holes (SMBHs) indicate that the two co-evolve (*e.g.* Kormendy & Richstone 1995; Magorrian *et al.* 1998; Ferrarese & Merritt 2000; Gebhardt *et al.* 2000; Graham *et al.* 2001). It has been suggested that galaxy-galaxy interactions, along with feedback from active galactic nuclei (AGN), form the foundation for SMBH-host galaxy co-evolution (*e.g.* Binney & Tabor 1995; Silk & Rees 1998; Kauffmann & Haehnelt 2000; Granato *et al.* 2001). The most massive galaxies in the universe, *e.g.* brightest cluster galaxies (BCGs), are a unique population in the co-evolution framework as their properties are also

correlated with the galaxy cluster, or group, in which they reside (*e.g.* Jones & Forman 1984; Dubinski 1998). Thus, BCGs are especially valuable for investigating galaxy formation and evolution processes in a cosmological context, and in this paper we discuss one rare BCG, IRAS 09104+4109 (hereafter I09), which may be providing vital clues about these processes.

Galaxy formation models typically segregate AGN feedback into a distinct early-time, radiatively-dominated quasar (QSO) mode (*e.g.* Springel *et al.* 2005; Hopkins *et al.* 2006) and a late-time, mechanically-dominated radio mode (*e.g.* Croton *et al.* 2006; Bower *et al.* 2006). During the quasar mode of feedback, it is believed that quasar radiation couples to gas within the host galaxy and drives strong winds which deprive the SMBH of additional fuel, regulating growth of black hole mass (*e.g.* Hopkins *et al.* 2005; Di Matteo *et al.* 2005). This phase is expected to be short-lived, resulting in the expulsion of gas from the host galaxy and

\* Email:cavagnolo@oca.eu

temporarily quenching star formation (e.g. Narayanan et al. 2006; Menci et al. 2008). Direct evidence of radiative AGN feedback has been elusive (see Veilleux et al. 2005, for a review), with only a handful of systems (e.g. Polletta et al. 2008; Feruglio et al. 2010) and low-redshift ellipticals (Schawinski et al. 2009) providing the strongest evidence to date that quasar feedback influences the host galaxy in the ways models predict.

At later times, when the nuclear accretion rate is sub-Eddington and quasar activity has ceased, SMBH launched jets regulate the growth of galaxy mass through prolonged and intermittent mechanical heating of a galaxy’s gaseous halo (e.g. Kereš et al. 2005; Dekel & Birnboim 2006). Direct evidence of mechanical AGN feedback is seen in the form of cavities, sound waves, and shocks found in the X-ray halos of many massive galaxies, particularly in the relatively dense intracluster medium (ICM) surrounding most BCGs (e.g. Fabian et al. 2000b; McNamara et al. 2000; Churazov et al. 2001; Forman et al. 2007; Sanders & Fabian 2008). Encouragingly, studies have shown AGN supply enough energy to offset most of the host halo radiative losses (e.g. Fabian et al. 2003; Birzan et al. 2004; Dunn & Fabian 2006) and that AGN activity is closely correlated with cluster core conditions (e.g. Cavagnolo et al. 2008a; Rafferty et al. 2008), both indicative of the feedback loop required in models.

Though models divide feedback into two generic modes, they still form a unified schema (e.g. Sijacki et al. 2007) with a continuous distribution of AGN luminosities (e.g. Hopkins & Hernquist 2009). However, how these modes interact, and what processes are involved in transitioning from one to the other, are still poorly understood, partly from a lack of observational constraints. This paper presents observational evidence of mechanical and radiative feedback from the AGN in I09, perhaps implying that it is, using the nomenclature of quasar-mode/radio-mode models, a “transition” object.

I09 is an uncommon, low-redshift ( $z = 0.4418$ ) ultraluminous infrared galaxy (ULIRG;  $L_{\text{IR}} \sim 10^{13} L_{\odot}$ ) residing at the center of the cool core galaxy cluster RX J0913.7+4056. Unlike most ULIRGs, I09 is the BCG in a rich galaxy cluster, but unlike most BCGs, the spectral energy distribution of I09 is dominated by a heavily obscured quasar: it has the optical spectrum of a Seyfert-2 with most of the bolometric luminosity emerging longward of  $1 \mu\text{m}$  (Kleinmann et al. 1988; Hines & Wills 1993; Fabian et al. 1994; Evans et al. 1998; Franceschini et al. 2000; Iwasawa et al. 2001). I09 also hosts a pair of highly-linear,  $\approx 60$  kpc long jets which are dramatically misaligned from the beaming direction of the quasar (Hines & Wills 1993; Hines et al. 1999, hereafter H93 and H99, respectively). Using data from the Chandra X-ray Observatory (CXO), we present the discovery of 1) X-ray halo cavities associated with the I09 jets, and 2) an X-ray excess lying along the misaligned quasar beaming direction which may be associated with an irradiated nebula in the I09 halo. From these discoveries, and using results in the lengthy I09 literature, we go on to suggest that I09 may be cycling between the dominant mode of feedback, providing a local example of how massive galaxies at higher redshifts evolve from quasar-mode into radio-mode.

The observations and data reduction are discussed in Section 2. The AGN-ICM interaction is discussed in Section 3, analysis of ICM cavities, the I09 nucleus, and X-ray halo excesses are given in Sections 4, 5, and 6. Interpretation of the results are given in Section 7, and a brief summary concludes the paper in Section 8. A  $\Lambda$ CDM cosmology with  $H_0 = 70 \text{ km s}^{-1} \text{ Mpc}^{-1}$ ,  $\Omega_M = 0.27$ , and  $\Omega_{\Lambda} = 0.73$  is adopted, for which a redshift of  $z = 0.4418$  corresponds to  $\approx 9.1$  Gyr for the age of the Universe,  $D_A \approx 5.72 \text{ kpc arcsec}^{-1}$ ,

and  $D_L \approx 2.45 \text{ Gpc}$ . The ICM mean molecular weight and adiabatic index are assumed to be  $\mu = 0.597$  and  $\gamma = 5/3$ , respectively.

## 2 OBSERVATIONS AND DATA REDUCTION

### 2.1 X-ray

A 77.2 ks CXO observation of I09 was taken in January 2009 with the ACIS-I instrument (ObsID 10445), and a 9 ks ACIS-S observation was taken in November 1999 (ObsID 509). Both datasets were reprocessed and reduced using CIAO and CALDB versions 4.2. X-ray events were selected using ASCA grades, and corrections for the ACIS gain change, charge transfer inefficiency, and degraded quantum efficiency were applied. The pileup percentage for both observations across the full bandpass is  $< 4\%$ , low enough that no correction or spectral modeling was applied. Point sources were located and excluded using WAVDETECT and verified by visual inspection. Light curves were extracted from a source-free region of each observation to look for flares, and time intervals with  $> 20\%$  of the mean background count rate were excluded. After flare exclusion, the final combined exposure time is 83 ks.

The point source-free, flare-free events files were reprojected to a common tangent point, summed, and used for imaging analysis. The astrometry of the ObsID 509 dataset was improved using an aspect solution created with the CIAO tool REPROJECT\_ASPECT and the positions of several field sources. After astrometry correction, the positional accuracy between both observations improved by  $\approx 0.4''$  and was comparable to the resolution limit of the ACIS detectors ( $\approx 0.492'' \text{ pix}^{-1}$ ). We refer to the final point source-free, flare-free, exposure-corrected images as the “clean” images.

Unless stated otherwise, the X-ray spectral analysis in this paper was performed over the energy range 0.7–7.0 keV with the  $\chi^2$  statistic in XSPEC 12.4 (Arnaud 1996) using an absorbed, single-component MEKAL model (Mewe et al. 1985) with metal abundance as a free parameter (Solar distribution of Anders & Grevesse 1989) and 90% confidence intervals. All spectral models had the Galactic absorbing column density fixed at  $N_{\text{H,Gal}} = 1.58 \times 10^{20} \text{ cm}^{-2}$  (Kalberla et al. 2005). The I09 nucleus emits strong Fe K $\alpha$  emission which affects spectral fitting, and for analysis of the ICM, the nucleus was excluded using a region twice the size of the 90% CXO point-spread function (PSF) enclosed energy fraction (EEF; see Section 5).

### 2.2 Radio

Between 1986 and 2000, I09 was observed with the Very Large Array (VLA) at multiple radio frequencies and resolutions. Archival VLA continuum observations were reduced using the Common Astronomy Software Applications (CASA) version 3.0. Flagging of bad data was performed using a combination of CASA’s FLAGDATA tool and manual inspection. Radio images were generated by Fourier transforming, cleaning, self-calibrating, and restoring individual radio observations. The additional steps of phase and amplitude self-calibration were included to increase the dynamic range and sensitivity of the radio maps. All sources within the primary beam and first side-lobe with fluxes  $\geq 5\sigma_{\text{rms}}$  were imaged to minimize the final image noise.

Resolved emission associated with I09 is detected at 1.4 GHz, 5.0 GHz, and 8.4 GHz, while a  $3\sigma$  upper limit of 0.84 mJy is established at 14.9 GHz. The combined 1.4 GHz image is the deepest

and reveals the most extended structure, thus our discussion regarding radio morphology is guided using this frequency. The deconvolved, integrated 1.4 GHz flux of the continuous extended structure coincident with I09, and having  $S_\nu \gtrsim 3\sigma_{\text{rms}}$ , is  $14.0 \pm 0.5$  mJy. A significant spur of radio emission extending northeast from the nucleus is also detected with flux  $0.21 \pm 0.07$  mJy.

Fluxes for unresolved emission at 74 MHz, 151 MHz, and 325 MHz were retrieved from VLSS (Cohen et al. 2007), 7C Survey (Riley et al. 1999), and WENSS (Rengelink et al. 1997), respectively. No formal detection is found in VLSS, however, an overdensity of emission at the location of I09 is evident. For completeness, we measured a flux for the potential source, but excluded the value during fitting of the radio spectrum. The radio spectrum from 151–8400 MHz for the full radio source (lobes, jets, and core) was fitted with the KP (Kardashev 1962; Pacholczyk 1970), JP (Jaffe & Perola 1973), and CI (Heavens & Meisenheimer 1987) synchrotron models using the code of Waters & Zepf (2005), which is based on the method of Carilli et al. (1991). The models primarily differ in their electron pitch-angle distribution and number of particle injection assumptions. The JP model (single electron injection, randomized but isotropic pitch-angle distribution) yields the best fit with  $\chi^2(\text{DOF}) = 4.91(3)$ , a break frequency of  $\nu_B = 12.9 \pm 1.0$  GHz, and a low-frequency ( $\nu < 2$  GHz) spectral index of  $\alpha = -1.10 \pm 0.09$ . The bolometric radio luminosity was approximated by integrating under the JP curve between  $\nu_1 = 10$  MHz and  $\nu_2 = 10,000$  MHz, giving  $L_{\text{radio}} = 1.09 \times 10^{42}$  erg s $^{-1}$ . Repeating the above analysis using only radio lobe emission at 1.4 GHz, 5.0 GHz, and an 8.4 GHz upper limit gives a poorly constrained best-fit JP model with break frequency  $\nu_B = 1.3 \pm 1.1$  GHz and spectral index  $\alpha = -1.65 \pm 0.30$ . The radio spectra and best-fit models are shown in Figure 1.

### 3 AGN-HALO INTERACTION

Unsmoothed and unsharp masked 0.5–10.0 keV X-ray images of I09 are shown in Figure 2. Several systematic features are present in the unprocessed image which become pronounced structures in the unsharp masked image: 1) an arc of emission northwest of the nucleus, 2) a surface brightness depression directly southeast of the arc, 3) a northeast skewing of the nuclear emission, and 4) an edge-like feature southeast of the core with a faint surface brightness depression below it. All of the structures lie along the radio jet axis suggesting interaction between the AGN and ICM.

To better reveal ICM substructure, a 0.5–7.5 keV X-ray image made from the clean data was adaptively smoothed with a 1'' Gaussian and residual images were made by subtracting various smooth surface brightness models. A primary concern with residual imaging is that differences in the model and source ellipticities can create artifacts reminiscent of cavities, making it difficult to interpret the physical significance of faint residual structures. Thus, in Figure 3, we present three residual images created from three models with varying degrees of ellipticity.

The first residual image was created by fitting the 1D radial X-ray surface brightness profile with a double  $\beta$ -model (Cavaliere & Fusco-Femiano 1978) and subtracting its azimuthally symmetric 2D analog (model-A) from the clean image. The central source was excluded during fitting, hence its prominence in the residual image. For the second and third residual images, the 2D X-ray surface brightness isophotes of the clean image were fitted using the IRAF tool ELLIPSE. The second residual image results from a model which had ellipticity ( $\epsilon$ ), position angle ( $\phi$ ), and cen-

teroid ( $C$ ) as free parameters (model-B). The model for the third residual image (model-C) had  $\epsilon$ ,  $\phi$ , and  $C$  fixed to their mean values exterior to the substructure (see Figure 4).

In all three images, the surface brightness depressions northwest and southeast of the nucleus are resolved into cavities, and excesses to the north, east, and west of the core are evident. The presence of excesses raises the concern that they have influenced the isophotal fitting. We explored this possibility by masking the excesses during all phases of fitting and found no significant differences between the resulting residual images and those shown in Figure 3. We also tried removing the excesses from the X-ray images and repeating the analysis, but again found no significant differences in the resulting images. The cavities and excesses persist in spite of our best efforts to remove them and we conclude that these are real features of I09.

To assess the statistical significance of the substructures, we used two methods, the results of which are given in Table 1. For method-1, we measured the ratio of the surface brightness of each substructure to the value of the model-B isophotes over the same radial range (see Wise et al. 2007, for a similar approach). In method-2, we compared the surface brightness in 5° wedges around an annulus centered on the nucleus with width equal to the radial size of each structure. On average, the substructures have significance of  $5.3\sigma$  with all meeting the formal detection requirement of being  $> 3\sigma$ .

Shown in more detail in Figure 5 is the model-B residual image overlaid with radio contours. Though the substructures are relatively weak, the nice correlation between the X-ray and radio morphologies strongly indicates they originate from a jet-halo interaction. The northern and western excesses (NEx and WEx, respectively) appear to form a tenuous, arc-like filament of gas possibly displaced by the northwest radio jet, and several knots of significant radio emission coincide with the NEx-WEx base. The region between the NEx and nucleus is not of uniform depth, but it lies perfectly along the northwest jet forming a continuous cavity, and the same is true of the region along the southeast jet. At the base of the southeast jet, the radio emission narrows at the same location an arm of X-ray emission impinges on the jet, forming what appears to be a bottleneck. A detailed analysis of the cavities is provided in Section 4.

There are additional deficits east of the eastern excess (EEx) and south of the WEx which lie along off the nuclear beaming axis and are further from the core than the detected cavities. The extra decrements are unassociated with any radio emission and their physical significance is unclear. Fabian & Crawford (1995) previously reported detecting a “hole” in a ROSAT/HRI image of I09, but, when overlaid on the CXO residual image, the hole is not associated with the cavities, and neither the cavities nor the hole are seen in a longer follow-up HRI observation.

Based on the I09 scattered UV and polarized emission properties, H93 and H99 suggest the AGN which produced the large-scale jets has recently ( $\sim 70,000$  yr) been reoriented to a new beaming direction roughly orthogonal to the previous beaming axis and close to our line-of-sight. Interestingly, the new AGN axis suggested by H93/H99 is coincident with the EEx, the radio spur emanating northeast from the nucleus, a cone of scattered UV radiation, an ionized optical nebula, and highly polarized optical emission, all of which are highlighted in Figure 5. Thus, we suspect that beamed nuclear radiation is interacting with the X-ray halo producing the EEx, a possibility discussed in Sections 5 and 6.



#### 4 ICM CAVITIES AND AGN MECHANICAL FEEDBACK

AGN induced X-ray cavities are a well-known feature of many massive galaxies and provide a reliable method for estimating the  $P_V$  work, and hence mechanical energy output, expended by an AGN (see [McNamara & Nulsen 2007](#), for a review). I09 is unique in that it is currently the only quasar-dominated system (and highest redshift object) with a cavity detection. Below, we first quantify the radial properties of the ICM (a requisite for cavity analysis) and then present discussion of the outburst energetics.

##### 4.1 ICM Radial Profiles

The radial profiles discussed in this section are shown in Figure 6. Radial temperature ( $kT_X$ ) and abundance ( $Z$ ) profiles were created by extracting spectra from circular annuli centered on the cluster X-ray peak with each annulus containing 2500 and 5000 source counts, respectively. Background spectra were extracted from reprocessed CALDB blank-sky backgrounds matched to each observation and renormalized using the ratio of blank-sky and observation 9.5–12 keV flux for an off-axis, source-free region. A fixed background component was included during spectral analysis to account for the spatially-varying Galactic foreground (see [Vikhlinin et al. 2005](#) and [Cavagnolo et al. 2008b](#) for method). Source spectra were grouped to 25 counts per energy channel and fit using the model described in Section 2.1. A deprojected temperature profile was generated using the PROJCT model in XSPEC, but it does not significantly differ from the projected profile which is used in all subsequent analysis.

A gas density profile was derived from a radial surface brightness profile extracted from concentric  $1''$  wide circular annuli centered on the cluster X-ray peak. Using the surface brightness and temperature profiles, the deprojected electron density ( $n_e$ ) profile was calculated using the technique of [Kriss et al. \(1983\)](#) which incorporates spectral count rates and best-fit normalizations to account for variations of gas emissivity (see [Cavagnolo et al. 2009](#), for method details). Gas density errors were estimated from 10,000 Monte Carlo simulations of the surface brightness profile. Total gas pressure was calculated as  $P = nkT_X$ , where  $n = 2.3n_H$  and  $n_H = n_e/1.2$  for a fully ionized plasma. For completeness, profiles of entropy ( $K = kT_X n_e^{-2/3}$ ), cooling time ( $t_{cool} = 3nkT_X [2n_e n_H \Lambda(T, Z)]^{-1}$ ), and enclosed X-ray luminosity ( $L_X$ ) were also produced. The  $\Lambda(T, Z)$  in  $t_{cool}$  are cooling functions derived from the best-fit spectral model for each annulus of the temperature profile and were linearly interpolated onto the grid of the higher resolution density profile. The uncertainties for each profile were propagated from the individual parameters and summed in quadrature.

##### 4.2 Outburst Energetics

Cavity volumes,  $V$ , were calculated by approximating each void in the X-ray image with a right circular cylinder projected onto the plane of the sky along the cylinder radial axis. The lengthwise axis of the cylinders were assumed to lie in a plane that passes through the central AGN and is perpendicular to our line-of-sight. A systematic uncertainty of 10% was assigned to the cavity volumes to account for unknown projection effects. The energy in each cavity,  $E_{cav} = \gamma PV / (\gamma - 1)$ , was estimated by assuming the contents are a relativistic plasma ( $\gamma = 4/3$ ), and then integrating the total ICM pressure over the surface of each cylinder. We assume the cavity

ages are equal to the time required for the jets to displace gas at the ambient sound speed ([Birzan et al. 2004](#)):

$$t_{sonic} = D \sqrt{\frac{\mu m_H}{\gamma k T_X}} \quad (1)$$

where  $\gamma$  and  $\mu$  are the ICM adiabatic index and mean molecular weight,  $m_H$  [g] is the mass of hydrogen, and  $D$  [cm] is the distance the AGN outflow has traveled to create each cavity, which was set to the cylinder lengths and not their midpoints, as is common. The AGN power required to make each cavity is thus  $P_{cav} = E_{cav} / t_{sonic}$ . Properties of the individual cavities are listed in Table 2.

The total cavity energy and power are estimated at  $E_{cav} = 5.11 (\pm 1.33) \times 10^{59}$  erg and  $P_{cav} = 3.05 (\pm 1.03) \times 10^{44}$  erg s $^{-1}$ , respectively. Radio power has been shown to be a reasonable surrogate for estimating mean jet power ([Birzan et al. 2008](#)), though with considerable scatter. Thus, we checked the  $P_{cav}$  calculation using the [Cavagnolo et al. \(2010\)](#)  $P_{cav}$ - $L_{radio}$  scaling relations which give  $P_{cav} \approx 2\text{--}6 \times 10^{44}$  erg s $^{-1}$ , in agreement with the X-ray measurements, suggesting there is nothing unusual about the jet radiative efficiency. Compared with other systems hosting cavities (e.g. [Birzan et al. 2004](#); [Dunn & Fabian 2008](#)), I09 is not unusually powerful, residing near the middle of the cavity power distribution.

Since AGN have been implicated as a key component in regulating late-time galaxy growth, of interest is a comparison of the AGN energy output and the cooling rate of the host X-ray halo. The cooling radius of the halo was set at the radius where the ICM cooling time is equal to  $H_0^{-1}$  at the redshift of I09. We calculate  $R_{cool} = 128$  kpc, and measure an unabsorbed bolometric luminosity within this radius of  $L_{cool} = 1.61_{-0.20}^{+0.25} \times 10^{45}$  erg s $^{-1}$ . If all of the cavity energy is thermalized over  $4\pi$  sr, then  $\approx 20\%$  of the energy radiated away by gas within  $R_{cool}$  is replaced by energy in the observed outburst. Assuming the mean ICM cooling rate does not vary significantly on a timescale of  $\sim 1$  Gyr, this idealized scenario implies that 5 similar power AGN outbursts will balance the cooling losses of the cluster halo. Similar results are found for many other BCGs (e.g. [Rafferty et al. 2006](#)), again highlighting that the I09 outburst mechanical properties are not atypical.

##### 4.3 Constraints on Shock Energy

The energetics calculations given above are often assumed to be a good estimate of the physical quantity jet power,  $P_{jet}$ . However, neither  $P_{cav}$  nor  $P_{jet}$  account for energy which may be imparted to shocks. But, the radio source synchrotron age ( $t_{sync}$ ) and cavity ages are useful in addressing this issue. Assuming  $t_{sync}$  is an accurate measure of a cavity system's dynamical age, if  $t_{sync}$  is less than  $t_{sonic}$ , one might infer that an AGN outflow is strongly driven, possibly supersonic. Were it not, the radio-loud plasma should radiate away much of its energy (neglecting re-acceleration) and be mostly radio-quiet prior to reaching the end of an observed jet. The implication being that during cavity creation, some jet kinetic energy may be imparted to shocks, making  $E_{cav}$  a lower limit on the total AGN energy output.

We first point-out that there are no resolved discontinuities in the radial ICM temperature, density, or pressure profiles to suggest the presence of large-scale shocks. Other authors have also noted the I09 emission line properties are inconsistent with shock excitation ([Crawford & Vnderriest 1996](#); [Tran et al. 2000](#)). But, detecting weak, small-scale shocks in the X-ray sometimes requires very high signal-to-noise (SN), and the nebular regions used to study shock excitation are far from the jets and may not be indicative of gas dynamics close to the outflow.

The radio source synchrotron age was constrained using the radio spectra presented in Section 2.2. Assuming inverse-Compton scattering and synchrotron emission are the dominant radiative mechanisms, the time since last acceleration for an isotropic particle population is (Slee et al. 2001)

$$t_{\text{sync}} = 1590 \left( \frac{B^{1/2}}{B^2 + B_{\text{CMB}}^2} \right) [v_B(1+z)]^{-1/2} \text{ Myr} \quad (2)$$

where  $B$  [ $\mu\text{G}$ ] is magnetic field strength,  $B_{\text{CMB}} = 3.25(1+z)^2$  [ $\mu\text{G}$ ] is a correction for inverse-Compton losses to the cosmic microwave background,  $v_B$  [GHz] is the radio spectrum break frequency, and  $z$  is the dimensionless source redshift. Note that energy losses to adiabatic expansion have been neglected (Scheuer & Williams 1968). We assume  $B$  is not significantly different from the equipartition magnetic field strength,  $B_{\text{eq}}$  (see Bîrzan et al. 2008, regarding the validity of this assumption), which is derived from the minimum energy density condition as (Milewicz 1980)

$$B_{\text{eq}} = \left[ \frac{6\pi c_{12}(\alpha, v_1, v_2) L_{\text{radio}} (1+k)}{V\Phi} \right]^{2/7} \mu\text{G} \quad (3)$$

where  $c_{12}(\alpha, v_1, v_2)$  is a dimensionless constant (Pacholczyk 1970),  $L_{\text{radio}}$  [ $\text{erg s}^{-1}$ ] is the integrated radio luminosity from  $v_1$  to  $v_2$ ,  $k$  is the dimensionless ratio of lobe energy in non-radiating particles to that in relativistic electrons,  $V$  [ $\text{cm}^3$ ] is the radio source volume, and  $\Phi$  is a dimensionless radiating population volume filling factor. Synchrotron age as a function of  $k$  and  $\Phi$  for the full source, and lobes only, are shown in Figure 7. For various combinations of  $k$  and  $\Phi$ , the ages range from  $\approx 2$ –30 Myr, not atypical of other BCG radio sources (e.g. Bîrzan et al. 2008).

A comparison of the radio source and cavity ages reveals  $t_{\text{sonic}} \gtrsim 42$  Myr and  $t_{\text{sync}} \lesssim 30$  Myr, the situation where a supersonic outflow may be present. Relative to the ICM sound speed, the velocity needed to reach the end of the radio jet in 30 Myr requires a Mach number of  $\approx 1.7$ . The energy possibly channeled into shocks was crudely estimated by setting  $t_{\text{sonic}} = 30$  Myr and adjusting the pressure at the end of the cavities by the Mach number,  $\Delta P_{\text{cav}} = \Delta P / \Delta t$  and  $\Delta P \propto M^3$ , giving  $P_{\text{jet}} \sim 10^{45} \text{ erg s}^{-1}$  and  $E_{\text{cav}} \sim 10^{60} \text{ erg}$  for a 30 Myr duration. These are large values for an AGN outburst, but the inferred Mach number is not outside the range of observed values in other systems (e.g. Forman et al. 2005; McNamara et al. 2005; Wise et al. 2007; Croston et al. 2009). If the midpoints of the cavities are instead used for calculating cavity ages, then  $t_{\text{sonic}} \approx 30$  Myr and the outflow does not need to be supersonic. Given the uncertainties in determination of the cavity and radio source ages, there exists a reasonable possibility of weak ICM shocking.

## 5 THE I09 NUCLEUS

At the heart of the AGN outburst is the complex nucleus of I09. Below, we analyze the nucleus for the later purpose of investigating the irradiation of the ICM and to help constrain which processes may be fueling the AGN activity.

### 5.1 Spectral Properties

The centroid and extent of the nuclear X-ray source were determined with the CIAO tool `wavdetect` and confirmed with visual inspection of a hardness ratio map calculated as  $HR =$

$f(2.0\text{--}9.0 \text{ keV})/f(0.5\text{--}2.0 \text{ keV})$ , where  $f$  is the flux in the denoted energy band. Comparison of surface brightness profiles for the nuclear source and normalized *CXO* PSF specific to the nuclear source median photon energy and off-axis position confirm the source is point-like. A source extraction region was defined using the 90% EEf of the PSF (effective radius of  $1.16''$ ), and an identical segmented elliptical annulus with 5 times the area of the source region was used for extracting a background spectrum. The background annulus was broken into segments to avoid the regions of excess X-ray emission discussed in Section 3. The *HR* map and extraction regions are shown in Figure 8.

For each *CXO* observation, source and background spectra were extracted using the CIAO tool `psextract` and grouped to have 20 counts per energy channel. Previous studies have shown that the nucleus is obscured by a Compton thick screen, and that the X-ray emission is in fact reflected quasar radiation with a strong Fe  $K\alpha$  fluorescence line ( $E_{\text{rest}} = 6.4 \text{ keV}$ ) component (e.g. Franceschini et al. 2000; Iwasawa et al. 2001). Thus, the 1999 and 2009 spectra (hereafter SP99 and SP09, respectively) were fitted separately in XSPEC over the energy range 0.5–7.0 keV with an absorbed PEXRAV model (Magdziarz & Zdziarski 1995) plus three Gaussians to account for the Fe  $K\alpha$  line and two additional line-like features around 0.8 keV and 1.3 keV (see also Iwasawa et al. 2001). Note that the iridium edge feature of the ACIS detector is at  $\approx 2.0 \text{ keV}$ , far from any of the observed emission features.

The disk-reflection geometry employed in the PEXRAV model is not ideal for fitting reflection from a Compton-thick torus (Murphy & Yaqoob 2009), but no other suitable XSPEC model is currently available. Hence, only the reflection component of the PEXRAV model was used and the power law had no high energy cut-off. Fitting separate SP99 and SP09 models allowed for source variation in the decade between observations, however  $\Gamma$  was poorly constrained for SP99 and thus fixed at the SP09 value. Using constraints from Taniguchi et al. (1997) and Tran et al. (2000), the model parameters for reflector abundance and source inclination were fixed at  $1.0 Z_{\odot}$  and  $i = 50^\circ$ , respectively. The best-fit model parameters are given in Table 4, and the background-subtracted spectra overplotted with the best-fit models are presented in Figure 9.

The 2–10 keV *reflected* flux of our best-fit model without Galactic absorption is  $4.24_{-0.55}^{+0.57} \times 10^{-13} \text{ erg s}^{-1} \text{ cm}^{-2}$ , corresponding to a 2–10 keV rest-frame luminosity  $L_{2-10}^{\text{refl}} = 1.57_{-0.19}^{+0.19} \times 10^{44} \text{ erg s}^{-1}$  and bolometric (0.01–100.0 keV) luminosity  $L_{\text{bol}}^{\text{refl}} = 4.20_{-0.47}^{+0.49} \times 10^{45} \text{ erg s}^{-1}$ . Since the reflection component is the only directly measured quantity, the intrinsic quasar luminosity,  $L_{\text{QSO}}$ , can only be inferred. If the reflector scattering albedo is  $\eta \lesssim 0.1$ , a reasonable assumption for systems with properties similar to I09 (Murphy & Yaqoob 2009), and less than half of the reflector solid angle is exposed to our line of sight, then the intrinsic luminosity may be more than 20 times the calculated bolometric value. Thus, we hereafter assume  $L_{\text{QSO}} \approx 8 \times 10^{46} \text{ erg s}^{-1}$ , consistent with I09's 0.3–70  $\mu\text{m}$  luminosity of  $\approx 5 \times 10^{46} \text{ erg s}^{-1}$  which is attributed to dust reprocessing of quasar radiation (Kleinmann et al. 1988, H99).

Strong Mg, Ne, S, and Si  $K\alpha$  fluorescence lines at  $E < 3.0 \text{ keV}$ , in addition to photoionized Fe L-shell lines, can be present in reflection spectra (Band et al. 1990; George & Fabian 1991). Given that the nucleus is extremely luminous and that the spectrum is reflection-dominated, we find it likely that the soft X-ray emission fitted by the two separate Gaussians represents some combination of these emission lines. Using a solar abundance thermal component in place of the two low-energy Gaussians yielded a statistically

worse fit: the model systematically underestimated the 1–1.5 keV flux and overestimated the 2–4 keV flux. Leaving the thermal component abundance as a free parameter resulted in  $0.1 Z_{\odot}$ , *i.e.* the thermal component tended toward a featureless, skewed-Gaussian.

Our measurement of the Fe  $K\alpha$  line equivalent width ( $EW_{K\alpha}$ ) agrees with previous studies which found  $EW_{K\alpha} \lesssim 1$  keV (Franceschini et al. 2000; Iwasawa et al. 2001; Piconcelli et al. 2007), but the large uncertainties prevent us from determining if  $EW_{K\alpha}$  has varied since 1998. Our  $EW_{K\alpha}$  measurement is also consistent with AGN models and observations which show that  $EW_{K\alpha} \gtrsim 0.5$  keV is correlated with  $\Gamma \gtrsim 1.7$ , and implies that the column density of the reflecting material is  $N_{H,\text{ref}} \sim 10^{24} \text{ cm}^{-2}$  (Matt et al. 1996; Nandra et al. 1997; Zdziarski et al. 1999; Fabian et al. 2000a; Guainazzi et al. 2005). The high inferred  $N_{H,\text{ref}}$  is relevant to the properties of the nuclear obscurer, which we discuss next.

## 5.2 Nuclear Obscuration

Conclusions reached in previous studies regarding the I09 nucleus have relied on a *BeppoSAX* hard X-ray detection which has been interpreted as emission transmitted through a moderately Compton-thick obscuring screen, *i.e.*  $N_{H,\text{obs}} > 10^{24} \text{ cm}^{-2}$  (Franceschini et al. 2000; Iwasawa et al. 2001). This result has been questioned by Piconcelli et al. (2007), and we confirmed the original *BeppoSAX* analysis of Franceschini et al. (2000) by analyzing the archival *BeppoSAX* I09 observation with SAXDAS version 2.3.1 using the calibration data, cookbook, and epoch appropriate response functions available from HEASARC<sup>1</sup>. In agreement with their analysis, we measure a 15–80 keV count rate of  $0.106 \pm 0.055 \text{ ct s}^{-1}$  for the PDS hard X-ray instrument, and estimate 10–200 keV and 20–100 keV fluxes of  $f_{10-200} = 2.09^{+1.95}_{-1.95} \times 10^{-11} \text{ erg s}^{-1} \text{ cm}^{-2}$  and  $f_{20-100} = 1.10^{+1.57}_{-1.63} \times 10^{-11} \text{ erg s}^{-1} \text{ cm}^{-2}$ .

Extrapolating the best-fit model for the *CXO* data out to 10–80 keV reveals statistically acceptable agreement with the PDS data (see Figure 9). The best-fit model 10–200 keV flux is  $f_{10-200} = 8.15^{+0.21}_{-0.19} \times 10^{-12} \text{ erg s}^{-1} \text{ cm}^{-2}$ , which is not formally different from the *BeppoSAX* 10–200 keV flux. However, if transmitted hard X-ray emission is present below the 7.0 keV cut-off selected for spectral analysis, the best-fit power-law component might be artificially shallower than its intrinsic value, and the hard X-ray flux will thus be overestimated. We tested this possibility by simulating absorbed power-law spectra and found that for  $\Gamma \geq 1.7$ , column densities  $> 3 \times 10^{24} \text{ cm}^{-2}$  are sufficient to suppress emission below 7 keV. Consistent with this result, addition of an absorbed, power-law component to the modeling of the real data lowered  $\chi^2$  (best-fit  $N_{H,\text{obs}} = 3 \times 10^{24} \text{ cm}^{-2}$  and  $\Gamma = 1.7$ ), but with no improvement to the goodness of fit derived from 10,000 Monte Carlo simulations.

That we find no need for an additional hard X-ray component does not contradict the well-founded conclusion that I09 harbors a Compton-thick quasar. On the contrary, the measured  $EW_{K\alpha}$  suggests reflecting column densities of  $N_{H,\text{ref}} \sim 1\text{--}5 \times 10^{24} \text{ cm}^{-2}$  (Leahy & Creighton 1993; Guainazzi et al. 2005; Comastri et al. 2010). Assuming the obscuring nuclear material is nearly homogeneous, then  $N_{H,\text{ref}} \approx N_{H,\text{obs}}$  and our results are consistent with the presence of a moderately Compton-thick obscuring screen.

The *BeppoSAX*/PDS full-width half maximum field is quite large ( $\approx 1^\circ$ ), raising the concern that the hard X-ray emission

is not associated with I09. The X-ray instruments on-board *INTEGRAL* and *Swift* provide a check of this possibility. I09 was not detected in the *INTEGRAL*/IBIS Extragalactic AGN Survey (Bassani et al. 2006), and our re-analysis of archival *INTEGRAL* data yielded a 20–100 keV  $3\sigma$  upper limit of  $f_{20-100} = 5.70 \times 10^{-11} \text{ erg s}^{-1} \text{ cm}^{-2}$ , higher than the 20–100 keV *BeppoSAX*/PDS measured flux and consistent with a  $z = 0.44$  source which would not be detected in the IBIS Survey. I09 was also not detected in the 22 month *Swift*/BAT Survey (Tueller et al. 2010) which has a 14–195 keV  $4.8\sigma$  detection limit of  $2.2 \times 10^{-11} \text{ erg s}^{-1} \text{ cm}^{-2}$ , higher than the *BeppoSAX* 14–195 keV flux. Assuming the *INTEGRAL* and *Swift* upper limits are valid for an  $\approx 1^\circ$  region around I09, the lack of detected hard X-ray sources suggests the *BeppoSAX* detection did not originate from a *brighter* off-axis source.

## 6 ICM EXCESSES AND AGN RADIATIVE FEEDBACK

### 6.1 Spectral Analysis of Excesses

Having constrained the properties of the nucleus and mechanical outflow, it is now possible to analyze the NEx, WEx, and EEx ICM X-ray excesses (see Section 3) and evaluate their association with AGN feedback. A source spectrum was extracted for each excess, and a background spectrum was extracted from regions neighboring each excess which show minimal enhanced emission in the residual image (regions shown in Figure 10). The source regions were selected by moving out from the peak of each excess and finding the isocontour one pixel interior to where the residual normalized flux declined by more than a factor of two. This is an arbitrary choice made to ensure the “core” of the excesses was analyzed. For each region, the ungrouped source and background spectra were differenced within XSPEC and fitted with XSPEC’s modified Cash statistic (Cash 1979), appropriate for low-count, background-subtracted spectra (see XSPEC Manual Appendix B and Nousek & Shue 1989). Metal abundance was fixed at  $0.5 Z_{\odot}$  because the low-SN of each residual spectrum prohibited setting it as a free parameter. Varying the fixed abundance by  $\pm 0.2 Z_{\odot}$  changed the output temperatures and normalizations within the statistical uncertainties when  $0.5 Z_{\odot}$  was assumed. The best-fit spectral models are given in Table 3.

Analysis of the NEx residual spectrum was inconclusive due to extremely low-SN. However, the northern radio jet terminates in the NEx region, and the hardness ratio map shows a possible hot spot in this same area. It is possible the NEx results from the presence of a very hot thermal or non-thermal phase associated with the radio lobe. The WEx has a residual spectrum consistent with thermal emission from gas cooler than its surroundings, and is rather unremarkable apart from its unclear association with the outflow and the NEx.

For the EEx spectrum, no combination of thermal models was able to reproduce the flux associated with prominent emission features at  $E < 2$  keV, resulting in large systematic trends in the fit statistic residuals. The EEx thermal Fe  $K\alpha$  complex was also poorly fit because of an obvious asymmetry toward lower energies. To address these spectral features, the EEx was modeled with three Gaussians and a single thermal component. Comparison of  $\chi^2$  goodness of fits determined from 10,000 Monte Carlo simulations for the best-fit models with and without the Gaussians indicate the model with the Gaussians is preferred. In the next section we discuss the EEx further.

<sup>1</sup> <http://heasarc.nasa.gov/docs/sax>



## 6.2 Quasar Irradiation of the Halo

A zoom-in of the EEx is shown in Figure 11. As pointed-out in Section 3, the EEx is coincident with a number of multiwavelength emission features and the nearly line-of-sight nuclear beaming direction proposed by H93/H99. The one-sidedness of the 4.8 GHz contours in the direction of all the other emission features may indicate the presence of jet Doppler beaming, providing further circumstantial evidence that the quasar beaming axis is close to our line-of-sight. Russell et al. (2010) have demonstrated that the quasar in H1821+643 is capable of photoionizing gas up to 30 kpc from the nucleus, and we suspect a similar process may be occurring in I09 giving rise to the EEx. To test this hypothesis, we adopted the approach of Russell et al. (2010) by simulating reflection and diffuse spectra for the nebula and ICM coincident with the EEx using CLOUDY (Ferland et al. 1998).

The nebular gas density and ionization state were taken from Tran et al. (2000), while the initial ICM temperature, density, and abundance were set at 3 keV,  $0.04 \text{ cm}^{-3}$ , and  $0.5 Z_{\odot}$ , respectively. No Ca or Fe lines are detected from the nebula coincident with the EEx, possibly as a result of metal depletion onto dust grains (e.g. Donahue & Voit 1993), while strong Mg, Ne, and O lines are (Tran et al. 2000). Thus, a metal depleted, grain-rich, 12 kpc thick nebular slab was placed 15 kpc from an attenuated  $\Gamma = 1.7$  power law source with power  $8 \times 10^{46} \text{ erg s}^{-1}$  (see Section 5). Likewise, a  $17 \text{ kpc} \times 16 \text{ kpc}$  ICM slab was placed 19 kpc from the same source. The quasar radiation was attenuated using a 15 kpc column of density  $0.06 \text{ cm}^{-3}$ , abundance  $0.5 Z_{\odot}$ , and temperature 3 keV. The output models were summed, folded through the CXO responses using XSPEC, and only normalized to the observed EEx spectrum.

The EEx spectrum and the CLOUDY model are shown in Figure 12. The CLOUDY model shows reasonable agreement with the real spectrum, but the discrepancies around 1 keV suggest some emission line fluxes are incorrect. This could arise from inaccuracy of the initial values for the nebula abundance and ionization state, or, since projection effects are likely important, the irradiated slab may be closer to the quasar than we can constrain. The need to apply a normalization greater than 1 to match the data suggests the latter is likely the case. In the energy range 0.1–10.0 keV, the nebular emission lines which exceed thermal line emission originate from Si, Cl, O, F, K, Ne, Co, Na, and Fe and occur as blends around redshifted 0.4, 0.6, 0.9, and 1.6 keV. The energies and strengths of these blends nicely coincide with the  $E < 2 \text{ keV}$  emission humps in the EEx spectrum. The observed asymmetry of the EEx Fe K $\alpha$  emission blend around 4.5 keV originates from the rest-frame 6.4 keV Fe K $\alpha$  photoionized line of the ICM and not the nebula. The consistency of the irradiation model with the observed EEx spectrum strongly suggests that beamed quasar radiation is indeed responsible for the nature of the EEx, but whether the irradiation translates to heating of the gas is unclear.

## 7 INTERPRETATION

We have presented evidence that the AGN/QSO in I09 is interacting with its surroundings through the radiative and mechanical feedback channels, and this remarkable galaxy may be providing important clues about how AGN feedback fundamentally operates. But, because I09 is a very unique BCG, before we can interpret this object in a broader context, it is important to determine if the host cluster appears exceptional in any way, check for corroborating evidence of radiative quasar feedback, explore how the feedback

may have been fueled, and attempt to understand why the feedback mode may be evolving. In this section, we explore all of these issues. Hereafter, we assume that relativistic AGN emission, e.g. jets and beamed radiation, emerge along the spin axis of a SMBH.

### 7.1 Host Cluster Properties

The mean cluster temperature,  $T_{\text{cl}}$ , was defined as the ICM temperature within the core-excised aperture  $0.15\text{--}1.0 R_{500}$  where  $R_{500}$  is the radius where the average cluster density is 500 times the critical density for a spatially flat Universe. The cluster cool core was excluded using a region  $0.15 R_{500}$  in size (Maughan 2007). A source spectrum and weighted responses were created for the core-excised aperture, and a background spectrum was extracted from the reprocessed CALDB blank-sky backgrounds. The relations from Arnaud et al. (2002) were used to iteratively calculate  $R_{500}$  until three consecutive iterations produced  $T_{\text{cl}}$  values which agreed within the 68% confidence intervals. We measure  $T_{\text{cl}} = 7.54^{+1.76}_{-1.15} \text{ keV}$  corresponding to  $R_{500} = 1.16^{+0.27}_{-0.19} \text{ Mpc}$ , and the ratio of the hard-band (2.0–7.0 keV) to broadband (0.7–7.0 keV) temperature is consistent with unity, implying the cluster may not be a merger system (e.g. Cavagnolo et al. 2008b).

The cluster gas and gravitational masses were derived assuming hydrostatic equilibrium and using the deprojected radial electron density and temperature profiles. Because the radial profiles extend to  $\approx 0.25 R_{500}$ , the mass calculations below include significant extrapolation, and thus are crude estimates. Electron gas density was converted to total gas density as  $n_g = 1.92 n_e \mu m_H$ . To ensure continuity and smoothness of the radial log-space derivatives, the density profile was fitted with a double  $\beta$ -model, and the temperature profile was fitted with the 3D- $T(r)$  model of Vikhlinin et al. (2006). The total gas mass within  $R_{500}$  is  $\approx 5.2 (\pm 0.4) \times 10^{13} M_{\odot}$ , and the total gravitating mass is  $\approx 4.7 (\pm 0.9) \times 10^{14} M_{\odot}$ . The gas to gravitating mass ratio is thus  $0.11 \pm 0.02$ . Errors were estimated from 10,000 Monte Carlo realizations of the density and temperature profiles.

The I09 host cluster, RX J0913.7+4056, has a temperature, luminosity, and gas fraction consistent with flux-limited and representative cluster samples (Reiprich & Böhringer 2002; Pratt et al. 2009). Fitting the function  $K(r) = K_0 + K_{100}(r/100 \text{ kpc})^{\alpha}$  to the entropy profile reveals best-fit values of  $K_0 = 12.6 \pm 2.9 \text{ keV cm}^2$ ,  $K_{100} = 139 \pm 8 \text{ keV cm}^2$ , and  $\alpha = 1.71 \pm 0.10$  for  $\chi^2(\text{DOF}) = 3.0(49)$ , typical of cool core clusters and the population of  $K_0 < 30 \text{ keV cm}^2$  clusters that have a radio-loud AGN and multiphase gas associated with the BCG (Cavagnolo et al. 2008a; Rafferty et al. 2008; Cavagnolo et al. 2009; Sanderson et al. 2009). If one ignores the strange BCG at its heart, RX J0913.7+4056 appears to be morphologically and spectroscopically a typical massive, relaxed galaxy cluster. With no reason to suspect the host cluster is unique in anyway, it appears the peculiar nature of I09 does not arise from the galaxy residing in a special cluster.

### 7.2 Supplementary Evidence of Quasar Feedback

AGN have three primary channels for interacting with their environment – jets, non-relativistic winds, and radiation pressure – and it is suspected each channel dominates at different phases of a galaxy’s evolution. The jets and nucleus of I09 have clearly impacted the X-ray halo, and below we argue that winds and radiation may be affecting gas within the galaxy, indicating all three AGN

channels have very recently been active, further pointing to I09 as a rare transition object.

I09's status as a ULIRG, and its  $> 10^{42}$  erg s $^{-1}$  H $\alpha$  luminosity, would suggest that the galaxy hosts  $> 10^{10}$  M $_{\odot}$  of cold gas (e.g. Sanders et al. 1988; Edge 2001). On the contrary, the H $_2$  mass of I09 is  $\approx 3 \times 10^9$  M $_{\odot}$ , there is  $< 5 \times 10^7$  M $_{\odot}$  of cold dust, the hot dust mass is  $\approx 1 \times 10^9$  M $_{\odot}$ , and no polycyclic aromatic hydrocarbon or silicate absorption features are detected in the galaxy's IR spectrum, though the huge IR luminosity may dilute their signal (Taniguchi et al. 1997; Peeters et al. 2004; Sargsyan et al. 2008; Combes et al. 2010). In spite of being a ULIRG BCG in a cool core cluster, I09 appears to be relatively gas-poor with a low gas-to-dust ratio. One possible explanation is that outflows driven by non-relativistic winds, in which rapid and extensive dust formation are expected (Elvis et al. 2002), may be breaking apart the gas reservoirs (e.g. Hopkins & Elvis 2010). Integral field spectroscopy indicates the presence of a  $> 1000$  km s $^{-1}$  emission line outflow coincident with the I09 nucleus (Crawford & Vandersriest 1996), and the CO upper limit of Evans et al. (1998) and nominal detection by Combes et al. (2010) do not exclude the existence of a high-velocity ( $> 1500$  km s $^{-1}$ ) component which could result from wind-driven shocks (e.g. Feruglio et al. 2010).

Lapi et al. (2005) predict  $\approx 5\%$  of  $L_{\text{QSO}}$  goes into strong winds, suggesting the I09 quasar wind power may be  $\sim 10^{45}$  erg s $^{-1}$ . Conservatively assuming the quasar has been active for  $\sim 10^5$  yr, the total wind energy could be  $\sim 10^{57}$  erg. If the total I09 interstellar medium (ISM) gas mass is  $< 10^{10}$  M $_{\odot}$  and its mean temperature is  $< 5000$  K (consistent with the values presented above), the IGM thermal energy ( $\sim m_{\text{H}}^{-1} k T M_{\text{ISM}}$ ) will be  $< 10^{55}$  erg, 100 times less than the quasar wind energy. If this is the case, it is possible for small-scale, wind-driven shocks to form in the ISM, coupling ambient gas reservoirs to the quasar and potentially destroying accretion fuel.

Pressure from the quasar radiation field will also influence gas in the galaxy, and in systems like I09 where the dust content is high, the pressure may be more efficiently absorbed because the quasar Eddington luminosity is effectively lowered,  $\lambda_{\text{Edd}} = L_{\text{QSO}}(1.38 \times 10^{38} M_{\text{BH}})^{-1}$  erg s $^{-1}$  s M $_{\odot}$  (e.g. Laor & Draine 1993), where  $M_{\text{BH}}$  is black hole mass (see Section 7.3). In Figure 13 is a diagram presented in Fabian et al. (2009) showing obscuring column density as a function of  $\lambda_{\text{Edd}}$  for AGN host galaxies selected from the 9-month *Swift*/BAT Survey. The diagram is divided into regions where dusty obscuring clouds are either long-lived, expelled, or appear as dust lanes. I09 has  $\lambda_{\text{Edd}} \approx 0.55$  and in the  $N_{\text{H,obs}}-\lambda_{\text{Edd}}$  plane resides on the far-side of long-lived region nearer the expulsion region than most other systems of similar  $N_{\text{H,obs}}$ . Taken at face value, the implication is that gas with a sight line to the quasar may be subject to forces capable of accelerating dusty clouds away from the quasar, potentially depriving the quasar of additional fuel. However, this conclusion is at the mercy of our choice for  $M_{\text{BH}}$  and assumed  $L_{\text{QSO}}$ , i.e. if  $M_{\text{BH}} \geq 4 \times 10^9$  M $_{\odot}$  and  $L_{\text{QSO}} \sim 4 \times 10^{46}$  erg s $^{-1}$ , then  $\lambda_{\text{Edd}} < 0.08$ , pushing I09 deeper into the long-lived region of the  $N_{\text{H,obs}}-\lambda_{\text{Edd}}$  plane, though still with a higher  $\lambda_{\text{Edd}}$  than AGN of similar  $N_{\text{H,obs}}$ .

### 7.3 Fueling the Feedback

Assuming the nucleus hosts a single SMBH, an estimate of its mass,  $M_{\text{BH}}$ , is needed prior to investigating how the AGN feedback is fueled. We note that black hole mass estimates for BCGs are non-trivial and using scaling relations calibrated for lower mass systems

may result in  $M_{\text{BH}}$  being underestimated (e.g. Lauer et al. 2007; Dalla Bontà et al. 2009). We calculated  $M_{\text{BH}}$  using the Graham (2007) relations which rely on host galaxy  $[B, R, K]$ -band magnitudes. These magnitudes were collected from HyperLeda, SDSS, and 2MASS and corrected for extinction, redshift, and evolution using the relations of Cardelli et al. (1989) and Poggianti (1997). We find a  $M_{\text{BH}}$  range of  $0.5\text{--}5.2 \times 10^9$  M $_{\odot}$  and adopt the weighted mean value of  $1.1^{+4.1}_{-0.5} \times 10^9$  M $_{\odot}$  where the uncertainties span the lowest and highest  $1\sigma$  values of the individual estimates. The Eddington accretion rate, which is the maximal inflow rate of gas not expelled by radiation pressure, for a black hole of this mass is

$$\dot{M}_{\text{E}} = \frac{2.2}{\epsilon} \left( \frac{M_{\text{BH}}}{10^9 M_{\odot}} \right) \approx 23^{+91}_{-12} \text{ M}_{\odot} \text{ yr}^{-1} \quad (4)$$

where we use an accretion disk radiative efficiency of  $\epsilon = 0.1$ . Hereafter, we define normalized accretion rates as  $\dot{m} \equiv \dot{M}_{\text{acc}}/\dot{M}_{\text{E}}$ .

If mass accretion alone is the dominant power source for the feedback, and not, for example, SMBH spin (Meier 2002; McNamara et al. 2010), then  $P_{\text{cav}}$  and  $L_{\text{QSO}}$  are directly related to the gravitational binding energy released by matter accreting onto the SMBH. The aggregate cavity energy implies a total accreted mass of  $M_{\text{acc}} = E_{\text{cav}}/(\epsilon c^2)$  with a mean accretion rate of  $\dot{M}_{\text{acc}} = M_{\text{acc}}/t_{\text{sonic}}$  where  $\epsilon$  is a mass-energy conversion efficiency. Using the widely accepted  $\epsilon = 0.1$  (Frank et al. 2002), the mechanical outflow may have resulted from the accretion of  $2.9 (\pm 0.7) \times 10^6$  M $_{\odot}$  of matter at a rate of  $0.054 \pm 0.004$  M $_{\odot} \text{ yr}^{-1}$  or  $\dot{m} \approx 0.002$ . On the other hand, the mass accretion rate required to power the quasar is  $\dot{M}_{\text{acc}}^{\text{QSO}} = L_{\text{QSO}}/(\epsilon c^2) \approx 14$  M $_{\odot} \text{ yr}^{-1}$  or  $\dot{m} \approx 0.6$ .

The origin of gas driving the nuclear activity cannot be precisely known, but how the gas is accreted can be constrained. If the accretion flow feeding the SMBH is composed of the hot ICM, it can be characterized in terms of the Bondi accretion rate

$$\dot{M}_{\text{B}} = 0.013 K_{\text{B}}^{-3/2} \left( \frac{M_{\text{BH}}}{10^9 M_{\odot}} \right)^2 \approx 3.2^{+17.9}_{-2.5} \times 10^{-4} \text{ M}_{\odot} \text{ yr}^{-1} \quad (5)$$

where  $K_{\text{B}}$  [keV cm $^2$ ] is the mean entropy of gas within the Bondi radius and we have assumed  $K_{\text{B}} = K_0$ . Considering only the demands of the jets, the Bondi ratio of such an accretion flow is  $\dot{M}_{\text{acc}}/\dot{M}_{\text{B}} \approx 200^{+900}_{-100}$ , disturbingly large and implying highly efficient hot gas accretion. However, the Bondi radius for I09 is unresolved, and  $K_{\text{B}}$  is likely less than  $K_0$ . Assuming gas close to  $R_{\text{B}}$  is no cooler than one-third the central temperature, i.e.  $\approx 1$  keV, and that the black hole mass is underestimated, i.e.  $M_{\text{BH}} = 5.2 \times 10^9$  M $_{\odot}$ , for a Bondi ratio near unity,  $K_{\text{B}}$  needs to be less than 3 keV cm $^2$ , 4 times lower than  $K_0$ . In terms of entropy, gas cooling time is  $\propto K^{3/2} k T_{\text{X}}^{-1}$  (Donahue et al. 2006), which for  $K \sim 3$  keV cm $^2$  suggests the accreting material will have  $t_{\text{cool}} \approx 100$  Myr, a factor of  $\approx 3.5$  below the shortest ICM cooling time and of order the core free-fall time ( $t_{\text{ff}}$ ). But this creates the problems that the gas should fragment and form stars (since  $t_{\text{cool}} \sim t_{\text{ff}}$ ), and is disconnected from cooling at larger radii, breaking the feedback loop (Soker 2006).

If instead cold-mode accretion dominates (Pizzolato & Soker 2005), then the gas which becomes fuel for the AGN is distributed in the BCG halo and migrates to the bottom of the galaxy potential in the form of cold blobs and filaments (Pizzolato & Soker 2010). The cluster core hosting I09 resides in the  $K_0 \lesssim 30$  keV cm $^2$  regime in which thermal electron conduction is too inefficient to suppress widespread environmental cooling (Voit et al. 2008), allowing such cooling subsystems to form and be long-lived. Indeed, radial filaments and gaseous substructure within 30 kpc of I09 are seen down



to the resolution-limit of *HST* (Armus et al. 1999). This may indicate the presence of cooling, overdense regions similar to those expected in the cold-mode accretion model. Though Bondi accretion cannot be ruled out, it does not seem viable and the process of cold-mode accretion appears to be more consistent with the properties of I09's halo. These results are not in conflict with prevailing models of AGN fueling and suggest the mechanism which fueled the outburst need not be exotic.

#### 7.4 Evolution of the Feedback Mode?

Using galaxy formation models as a template, if I09 is an example of a transition object, then its nature may originate from evolution of the nuclear accretion properties. In the advection-dominated accretion flow model (Narayan & Yi 1995), for any given  $M_{\text{BH}}$ , the competition between AGN radiative and mechanical output may hinge on a critical accretion rate,  $\dot{m}_{\text{crit}}$ , which dictates when accretion disk winds suppress the formation of jets. When  $\dot{m} > \dot{m}_{\text{crit}}$ , accretion power is primarily radiated away, and when  $\dot{m} < \dot{m}_{\text{crit}}$ , accretion power is mostly removed in a mechanical outflow (Esin et al. 1997). The observational constraints on  $\dot{m}_{\text{crit}}$  are loose, but studies of Galactic X-ray binaries and clusters with cavities indicate  $\dot{m}_{\text{crit}} \sim 10^{-2}$  (e.g. Gallo et al. 2003; Narayan & McClintock 2008; McNamara et al. 2010). Not surprisingly, the normalized accretion rate needed to power the I09 quasar ( $\dot{m} \sim 1$ ) is well above  $\dot{m}_{\text{crit}}$ , while the accretion rate for the jets ( $\dot{m} \sim 10^{-3}$ ) is well below it. But, H93 argue that radio properties of the jets and nucleus indicate the misalignment between the beamed nuclear emission and the large-scale jets likely transpired no more than  $\sim 1$  Myr ago but no less than  $\sim 0.1$  Myr. So, if the nature of I09 is related to evolution of its accretion flow properties, a relatively rapid thousand-fold change in the normalized accretion rate may be hard to explain.

Interestingly, the beaming misalignment may provide a constraint on the scenario which led to such a dramatic change. The nuclear emission indicates an active quasar, so it may be that during a prior period of highly sub-Eddington accretion when the jets were launched, the black hole may have received a supercritical inflow of gas (a hypothesized fueling mechanism for high-redshift quasars, e.g. Volonteri & Rees 2005) that sent the accretion rate over  $\dot{m}_{\text{crit}}$ , turned it into a quasar, and quenched the jets. For a slowly-spinning black hole, an asymmetric supercritical accretion event can potentially produce dramatic changes in SMBH angular momentum and the orientation of its spin axis (Cavagnolo et al. 2010, in preparation), thereby producing the type of jet-beamed radiation misalignment observed in I09. Furthermore, this scenario fits nicely with the AGN spin-evolution model of Garofalo et al. (2010) which predicts the process of retrograde accretion will 1) produce SMBH's with low angular momentum and 2) coincides with the suppression of jets by disk winds, similar to what we speculate may be occurring in I09.

Another possible explanation for the properties of I09 is that there are multiple SMBHs in the nucleus (which will be tested with upcoming VLBA observations), each with its own accretion system and beaming axis: one quasar system, one jetted system. If there is only one SMBH and the jets and quasar are operating simultaneously, which we cannot definitively rule-out, it would be inconsistent with the widely-accepted picture of jets being associated with thick-disks and quasars with thin-disks. We also cannot neglect that the black hole spin axis might have been altered by a succession of misaligned accretion disks (e.g. King et al. 2005) or a merger induced "spin-flip" (Merritt & Ekers 2002). The latter is problematic, however, since SMBH mergers may eject the final

black hole from its host galaxy (e.g. Campanelli et al. 2007), and merging black hole spin axes may naturally align in gas-rich environments (Bogdanović et al. 2007). Further, since mergers have also been implicated in producing long-lived X-ray substructures like cold fronts or shocks (Markevitch & Vikhlinin 2007) and inducing ICM bulk motions that result in deformed radio sources (Simionescu et al. 2009) – characteristics I09 does not possess – in general, the influence of mergers on I09 is questionable. There are, however, several objects within a projected 80 kpc of the nucleus which may be companion galaxy remnants (Soifer et al. 1996; Armus et al. 1999), so mergers cannot be ruled out.

## 8 SUMMARY

In this paper we have shown that the quasar in IRAS 09104+4109 is interacting with its environment through both the mechanical and radiative feedback pathways. For the first time, we have a direct measurement of the radiative to mechanical feedback ratio in a single system, and may be peeking into the process of how massive galaxies at higher redshifts evolve from quasar-mode into radio-mode. If I09 is typical of transition objects, our results suggest that as these systems evolve they may cycle between quasar-mode/radio-mode before becoming FR-I's, or, that FR-I's occasionally become FR-II's when enough gas is accreted. It is essential to note that the radiative and mechanical properties of I09 are not atypical, and, taken individually, I09 appears to be: a normal BCG, a normal obscured quasar, and a normal radio galaxy. I09 just so happens to be all these things at once. The key results in this paper are:

- ICM cavities have been discovered which indicate an AGN outburst with total mechanical power and energy of  $P_{\text{cav}} \approx 3 \times 10^{44} \text{ erg s}^{-1}$  and  $E_{\text{cav}} \approx 5 \times 10^{59} \text{ erg}$ , respectively. Comparison of the radio source synchrotron age and cavity dynamical ages indicate that the AGN outflow may be supersonic, leading us to speculate that weak ICM shocking may have occurred, potentially driving the total AGN power and energy output up to  $\sim 10^{45} \text{ erg s}^{-1}$  and  $10^{60} \text{ erg}$ , respectively.
- Detection and modeling of an X-ray excess northeast of the nucleus, which is co-spatial with the quasar beaming direction and several multiwavelength emission features associated with the nucleus, strongly indicates quasar radiation is interacting with the ICM and a nebula in the same region.
- The mass accretion rates required to power the AGN suggest that the fuel feeding the SMBH was likely not accreted directly from the hot ICM, *i.e.* via the Bondi mechanism, but rather obtained through the accretion of cold blobs of gas surrounding the BCG, *i.e.* via cold-mode accretion.
- We argue that the presence of a quasar, interaction of the X-ray halo and jets, ostensible I09 gas-poorness, nuclear emission line outflow, high effective Eddington quasar luminosity, and misalignment of the large-scale radio jets and beamed radiation from the nucleus, suggest that I09 is cycling between a kinetic-dominated mode of feedback to a radiation-dominated mode. Among several possible explanations for the nature of I09, we speculate that the feedback mode may be evolving because of a rapid, supercritical accretion event (of unknown origin) which drove the nuclear accretion rate above a critical rate controlling the competition between disk winds and jets.

## ACKNOWLEDGMENTS

Support for this work was provided by the National Aeronautics and Space Administration through Chandra Award Number GO9-0143X issued by the Chandra X-ray Observatory Center, which is operated by the Smithsonian Astrophysical Observatory for and on behalf of the National Aeronautics Space Administration under contract NAS8-03060. MD and GMV acknowledge support through NASA LTSA grant NASA NNG-05GD82G. BRM thanks the Natural Sciences and Engineering Research Council of Canada for support. KWC acknowledges financial support from L'Agence Nationale de la Recherche (ANR) through grant ANR-09-JCJC-0001-01. KWC thanks Niayesh Afshordi, Alastair Edge, and Kazushi Iwasawa for helpful discussions, and Guillaume Belanger and Roland Walter for advice regarding *INTEGRAL* data analysis.

## REFERENCES

- Anders E., Grevesse N., 1989, *Geochim. Cosmochim. Acta*, 53, 197 [2](#)
- Armus L., Soifer B. T., Neugebauer G., 1999, *Ap&SS*, 266, 113 [9](#)
- Arnaud K. A., 1996, in *Astronomical Society of the Pacific Conference Series*, Vol. 101, *Astronomical Data Analysis Software and Systems V*, Jacoby G. H., Barnes J., eds., pp. 17–[2](#)
- Arnaud M., Aghanim N., Neumann D. M., 2002, *A&A*, 389, 1 [7](#)
- Band D. L., Klein R. I., Castor J. I., Nash J. K., 1990, *ApJ*, 362, 90 [5](#)
- Bassani L., Molina M., Malizia A., Stephen J. B., Bird A. J., Bazzano A., Bélanger G., Dean A. J., De Rosa A., Laurent P., Lebrun F., Ubertini P., Walter R., 2006, *ApJ*, 636, L65 [6](#)
- Binney J., Tabor G., 1995, *MNRAS*, 276, 663 [1](#)
- Birzan L., McNamara B. R., Nulsen P. E. J., Carilli C. L., Wise M. W., 2008, *ApJ*, 686, 859 [4, 5](#)
- Birzan L., Rafferty D. A., McNamara B. R., Wise M. W., Nulsen P. E. J., 2004, *ApJ*, 607, 800 [2, 4](#)
- Bogdanović T., Reynolds C. S., Miller M. C., 2007, *ApJ*, 661, L147 [9](#)
- Bower R. G., Benson A. J., Malbon R., Helly J. C., Frenk C. S., Baugh C. M., Cole S., Lacey C. G., 2006, *MNRAS*, 370, 645 [1](#)
- Campanelli M., Lousto C., Zlochower Y., Merritt D., 2007, *ApJ*, 659, L5 [9](#)
- Cardelli J. A., Clayton G. C., Mathis J. S., 1989, *ApJ*, 345, 245 [8](#)
- Carilli C. L., Perley R. A., Dreher J. W., Leahy J. P., 1991, *ApJ*, 383, 554 [3](#)
- Cash W., 1979, *ApJ*, 228, 939 [6](#)
- Cavagnolo K. W., Donahue M., Voit G. M., Sun M., 2008a, *ApJ*, 683, L107 [2, 7](#)
- , 2008b, *ApJ*, 682, 821 [4, 7](#)
- , 2009, *ApJS*, 182, 12 [4, 7](#)
- Cavagnolo K. W., McNamara B. R., Nulsen P. E. J., Carilli C. L., Jones C., Birzan L., 2010, *ApJ*, 720, 1066 [4](#)
- Cavaliere A., Fusco-Femiano R., 1978, *A&A*, 70, 677 [3](#)
- Churazov E., Brüggen M., Kaiser C. R., Böhringer H., Forman W., 2001, *ApJ*, 554, 261 [2](#)
- Cohen A. S., Lane W. M., Cotton W. D., Kassim N. E., Lazio T. J. W., Perley R. A., Condon J. J., Erickson W. C., 2007, *AJ*, 134, 1245 [3](#)
- Comastri A., Iwasawa K., Gilli R., Vignali C., Ranalli P., Matt G., Fiore F., 2010, *arXiv e-prints*: 1005.3253 [6](#)
- Combes F., Garcia-Burillo S., Braine J., Schinnerer E., Walter F., Colina L., 2010, *ArXiv e-prints* [8](#)
- Crawford C. S., Vanderriest C., 1996, *MNRAS*, 283, 1003 [4, 8, 21](#)
- Croston J. H., Kraft R. P., Hardcastle M. J., Birkinshaw M., Worrall D. M., Nulsen P. E. J., Penna R. F., Sivakoff G. R., Jordán A., Brassington N. J., Evans D. A., Forman W. R., Gilfanov M., Goodger J. L., Harris W. E., Jones C., Juett A. M., Murray S. S., Raychaudhury S., Sarazin C. L., Voss R., Woodley K. A., 2009, *MNRAS*, 395, 1999 [5](#)
- Croton D. J., Springel V., White S. D. M., De Lucia G., Frenk C. S., Gao L., Jenkins A., Kauffmann G., Navarro J. F., Yoshida N., 2006, *MNRAS*, 365, 11 [1](#)
- Dalla Bontà E., Ferrarese L., Corsini E. M., Miralda-Escudé J., Coccato L., Sarzi M., Pizzella A., Beifiori A., 2009, *ApJ*, 690, 537 [8](#)
- Dekel A., Birnboim Y., 2006, *MNRAS*, 368, 2 [2](#)
- Di Matteo T., Springel V., Hernquist L., 2005, *Nature*, 433, 604 [1](#)
- Donahue M., Horner D. J., Cavagnolo K. W., Voit G. M., 2006, *ApJ*, 643, 730 [8](#)
- Donahue M., Voit G. M., 1993, *ApJ*, 414, L17 [7](#)
- Dubinski J., 1998, *ApJ*, 502, 141 [1](#)
- Dunn R. J. H., Fabian A. C., 2006, *MNRAS*, 373, 959 [2](#)
- , 2008, *MNRAS*, 385, 757 [4](#)
- Edge A. C., 2001, *MNRAS*, 328, 762 [8](#)
- Elvis M., Marengo M., Karovska M., 2002, *ApJ*, 567, L107 [8](#)
- Esin A. A., McClintock J. E., Narayan R., 1997, *ApJ*, 489, 865 [9](#)
- Evans A. S., Sanders D. B., Cutri R. M., Radford S. J. E., Surace J. A., Solomon P. M., Downes D., Kramer C., 1998, *ApJ*, 506, 205 [2, 8](#)
- Fabian A. C., Crawford C. S., 1995, *MNRAS*, 274, L63 [3](#)
- Fabian A. C., Iwasawa K., Reynolds C. S., Young A. J., 2000a, *PASP*, 112, 1145 [6](#)
- Fabian A. C., Sanders J. S., Allen S. W., Crawford C. S., Iwasawa K., Johnstone R. M., Schmidt R. W., Taylor G. B., 2003, *MNRAS*, 344, L43 [2](#)
- Fabian A. C., Sanders J. S., Ettori S., Taylor G. B., Allen S. W., Crawford C. S., Iwasawa K., Johnstone R. M., Ogle P. M., 2000b, *MNRAS*, 318, L65 [2](#)
- Fabian A. C., Shioya Y., Iwasawa K., Nandra K., Crawford C., Johnstone R., Kunieda H., McMahon R., Makishima K., Murayama T., Ohashi T., Tanaka Y., Taniguchi Y., Terashima Y., 1994, *ApJ*, 436, L51 [2](#)
- Fabian A. C., Vasudevan R. V., Mushotzky R. F., Winter L. M., Reynolds C. S., 2009, *MNRAS*, 394, L89 [8, 23](#)
- Ferland G. J., Korista K. T., Verner D. A., Ferguson J. W., Kingdon J. B., Verner E. M., 1998, *PASP*, 110, 761 [7](#)
- Ferrarese L., Merritt D., 2000, *ApJ*, 539, L9 [1](#)
- Feruglio C., Maiolino R., Piconcelli E., Menci N., Aussel H., Lamastra A., Fiore F., 2010, *A&A*, 518, L155+ [2, 8](#)
- Forman W., Jones C., Churazov E., Markevitch M., Nulsen P., Vikhlinin A., Begelman M., Böhringer H., Eilek J., Heinz S., Kraft R., Owen F., Pahre M., 2007, *ApJ*, 665, 1057 [2](#)
- Forman W., Nulsen P., Heinz S., Owen F., Eilek J., Vikhlinin A., Markevitch M., Kraft R., Churazov E., Jones C., 2005, *ApJ*, 635, 894 [5](#)
- Franceschini A., Bassani L., Cappi M., Granato G. L., Malaguti G., Palazzi E., Persic M., 2000, *A&A*, 353, 910 [2, 5, 6](#)
- Frank J., King A., Raine D. J., 2002, *Accretion Power in Astrophysics: Third Edition*, Frank, J., King, A., & Raine, D. J., ed. [8](#)
- Gallo E., Fender R. P., Pooley G. G., 2003, *MNRAS*, 344, 60 [9](#)

- Garofalo D., Evans D. A., Sambruna R. M., 2010, *MNRAS*, 402, 820 [9](#)
- Gebhardt K., Bender R., Bower G., Dressler A., Faber S. M., Filippenko A. V., Green R., Grillmair C., Ho L. C., Kormendy J., Lauer T. R., Magorrian J., Pinkney J., Richstone D., Tremaine S., 2000, *ApJ*, 539, L13 [1](#)
- George I. M., Fabian A. C., 1991, *MNRAS*, 249, 352 [5](#)
- Graham A. W., 2007, *MNRAS*, 379, 711 [8](#)
- Graham A. W., Erwin P., Caon N., Trujillo I., 2001, *ApJ*, 563, L11 [1](#)
- Granato G. L., Silva L., Monaco P., Panuzzo P., Salucci P., De Zotti G., Danese L., 2001, *MNRAS*, 324, 757 [1](#)
- Guainazzi M., Matt G., Perola G. C., 2005, *A&A*, 444, 119 [6](#)
- Heavens A. F., Meisenheimer K., 1987, *MNRAS*, 225, 335 [3](#)
- Hines D. C., Schmidt G. D., Wills B. J., Smith P. S., Sowinski L. G., 1999, *ApJ*, 512, 145 [2](#)
- Hines D. C., Wills B. J., 1993, *ApJ*, 415, 82 [2](#)
- Hopkins P. F., Elvis M., 2010, *MNRAS*, 401, 7 [8](#)
- Hopkins P. F., Hernquist L., 2009, *ApJ*, 698, 1550 [2](#)
- Hopkins P. F., Hernquist L., Cox T. J., Di Matteo T., Martini P., Robertson B., Springel V., 2005, *ApJ*, 630, 705 [1](#)
- Hopkins P. F., Hernquist L., Cox T. J., Di Matteo T., Robertson B., Springel V., 2006, *ApJS*, 163, 1 [1](#)
- Iwasawa K., Fabian A. C., Ettori S., 2001, *MNRAS*, 321, L15 [2](#), [6](#)
- Jaffe W. J., Perola G. C., 1973, *A&A*, 26, 423 [3](#)
- Jones C., Forman W., 1984, *ApJ*, 276, 38 [1](#)
- Kalberla P. M. W., Burton W. B., Hartmann D., Arnal E. M., Bajaja E., Morras R., Pöppel W. G. L., 2005, *A&A*, 440, 775 [2](#)
- Kardashev N. S., 1962, *Soviet Astronomy*, 6, 317 [3](#)
- Kauffmann G., Haehnelt M., 2000, *MNRAS*, 311, 576 [1](#)
- Kereš D., Katz N., Weinberg D. H., Davé R., 2005, *MNRAS*, 363, 2 [2](#)
- King A. R., Lubow S. H., Ogilvie G. I., Pringle J. E., 2005, *MNRAS*, 363, 49 [9](#)
- Kleinmann S. G., Hamilton D., Keel W. C., Wynn-Williams C. G., Eales S. A., Becklin E. E., Kuntz K. D., 1988, *ApJ*, 328, 161 [2](#), [5](#), [16](#)
- Kormendy J., Richstone D., 1995, *ARA&A*, 33, 581 [1](#)
- Kriss G. A., Cioffi D. F., Canizares C. R., 1983, *ApJ*, 272, 439 [4](#)
- Laor A., Draine B. T., 1993, *ApJ*, 402, 441 [8](#)
- Lapi A., Cavaliere A., Menci N., 2005, *ApJ*, 619, 60 [8](#)
- Lauer T. R., Faber S. M., Richstone D., Gebhardt K., Tremaine S., Postman M., Dressler A., Aller M. C., Filippenko A. V., Green R., Ho L. C., Kormendy J., Magorrian J., Pinkney J., 2007, *ApJ*, 662, 808 [8](#)
- Leahy D. A., Creighton J., 1993, *MNRAS*, 263, 314 [6](#)
- Magdziarz P., Zdziarski A. A., 1995, *MNRAS*, 273, 837 [5](#)
- Magorrian J., Tremaine S., Richstone D., Bender R., Bower G., Dressler A., Faber S. M., Gebhardt K., Green R., Grillmair C., Kormendy J., Lauer T., 1998, *AJ*, 115, 2285 [1](#)
- Markevitch M., Vikhlinin A., 2007, *Phys. Rep.*, 443, 1 [9](#)
- Matt G., Brandt W. N., Fabian A. C., 1996, *MNRAS*, 280, 823 [6](#)
- Maughan B. J., 2007, *ApJ*, 668, 772 [7](#)
- McNamara B. R., Nulsen P. E. J., 2007, *ARA&A*, 45, 117 [4](#)
- McNamara B. R., Nulsen P. E. J., Wise M. W., Rafferty D. A., Carilli C., Sarazin C. L., Blanton E. L., 2005, *Nature*, 433, 45 [5](#)
- McNamara B. R., Rohanizadegan M., Nulsen P. E. J., 2010, *arXiv e-prints*: 1007.1227 [8](#), [9](#)
- McNamara B. R., Wise M., Nulsen P. E. J., David L. P., Sarazin C. L., Bautz M., Markevitch M., Vikhlinin A., Forman W. R., Jones C., Harris D. E., 2000, *ApJ*, 534, L135 [2](#)
- Meier D. L., 2002, *New Astronomy Review*, 46, 247 [8](#)
- Menci N., Fiore F., Puccetti S., Cavaliere A., 2008, *ApJ*, 686, 219 [2](#)
- Merritt D., Ekers R. D., 2002, *Science*, 297, 1310 [9](#)
- Mewe R., Gronenschild E. H. B. M., van den Oord G. H. J., 1985, *A&AS*, 62, 197 [2](#)
- Miley G., 1980, *ARA&A*, 18, 165 [5](#)
- Murphy K. D., Yaqoob T., 2009, *MNRAS*, 397, 1549 [5](#)
- Nandra K., George I. M., Mushotzky R. F., Turner T. J., Yaqoob T., 1997, *ApJ*, 477, 602 [6](#)
- Narayan R., McClintock J. E., 2008, *New A Rev.*, 51, 733 [9](#)
- Narayan R., Yi I., 1995, *ApJ*, 452, 710 [9](#)
- Narayanan D., Cox T. J., Robertson B., Davé R., Di Matteo T., Hernquist L., Hopkins P., Kulesa C., Walker C. K., 2006, *ApJ*, 642, L107 [2](#)
- Nousek J. A., Shue D. R., 1989, *ApJ*, 342, 1207 [6](#)
- Pacholczyk A. G., 1970, *Radio astrophysics. Nonthermal processes in galactic and extragalactic sources*, Pacholczyk A. G., ed. [3](#), [5](#)
- Peeters E., Spoon H. W. W., Tielens A. G. G. M., 2004, *ApJ*, 613, 986 [8](#)
- Piconcelli E., Fiore F., Nicastro F., Mathur S., Brusa M., Comastri A., Puccetti S., 2007, *A&A*, 473, 85 [6](#)
- Pizzolato F., Soker N., 2005, *ApJ*, 632, 821 [8](#)
- , 2010, *MNRAS*, 408, 961 [8](#)
- Poggianti B. M., 1997, *A&AS*, 122, 399 [8](#)
- Polletta M., Omont A., Berta S., Bergeron J., Stalin C. S., Petitjean P., Giorgetti M., Trinchieri G., Srianand R., McCracken H. J., Pei Y., Dannerbauer H., 2008, *A&A*, 492, 81 [2](#)
- Pratt G. W., Croston J. H., Arnaud M., Böhringer H., 2009, *A&A*, 498, 361 [7](#)
- Rafferty D. A., McNamara B. R., Nulsen P. E. J., 2008, *ApJ*, 687, 899 [2](#), [7](#)
- Rafferty D. A., McNamara B. R., Nulsen P. E. J., Wise M. W., 2006, *ApJ*, 652, 216 [4](#)
- Reiprich T. H., Böhringer H., 2002, *ApJ*, 567, 716 [7](#)
- Rengelink R. B., Tang Y., de Bruyn A. G., Miley G. K., Bremer M. N., Roettgering H. J. A., Bremer M. A. R., 1997, *A&AS*, 124, 259 [3](#)
- Riley J. M. W., Waldram E. M., Riley J. M., 1999, *MNRAS*, 306, 31 [3](#)
- Russell H. R., Fabian A. C., Sanders J. S., Johnstone R. M., Blundell K. M., Brandt W. N., Crawford C. S., 2010, *MNRAS*, 402, 1561 [7](#)
- Sanders D. B., Soifer B. T., Elias J. H., Madore B. F., Matthews K., Neugebauer G., Scoville N. Z., 1988, *ApJ*, 325, 74 [8](#)
- Sanders J. S., Fabian A. C., 2008, *MNRAS*, 390, L93 [2](#)
- Sanderson A. J. R., O’Sullivan E., Ponman T. J., 2009, *MNRAS*, 395, 764 [7](#)
- Sargsyan L., Mickaelian A., Weedman D., Houck J., 2008, *ApJ*, 683, 114 [8](#)
- Schawinski K., Lintott C. J., Thomas D., Kaviraj S., Viti S., Silk J., Maraston C., Sarzi M., Yi S. K., Joo S., Daddi E., Bayet E., Bell T., Zuntz J., 2009, *ApJ*, 690, 1672 [2](#)
- Scheuer P. A. G., Williams P. J. S., 1968, *ARA&A*, 6, 321 [5](#)
- Sijacki D., Springel V., di Matteo T., Hernquist L., 2007, *MNRAS*, 380, 877 [2](#)
- Silk J., Rees M. J., 1998, *A&A*, 331, L1 [1](#)
- Simionescu A., Roediger E., Nulsen P. E. J., Brüggén M., Forman W. R., Böhringer H., Werner N., Finoguenov A., 2009, *A&A*, 495, 721 [9](#)
- Slee O. B., Roy A. L., Murgia M., Andernach H., Ehle M., 2001,



- AJ, 122, 1172 [5](#)
- Soifer B. T., Neugebauer G., Armus L., Shupe D. L., 1996, AJ, 111, 649 [9](#)
- Soker N., 2006, New Astronomy, 12, 38 [8](#)
- Springel V., White S. D. M., Jenkins A., Frenk C. S., Yoshida N., Gao L., Navarro J., Thacker R., Croton D., Helly J., Peacock J. A., Cole S., Thomas P., Couchman H., Evrard A., Colberg J., Pearce F., 2005, Nature, 435, 629 [1](#)
- Taniguchi Y., Sato Y., Kawara K., Murayama T., Mouri H., 1997, A&A, 318, L1 [5](#), [8](#)
- Tran H. D., Cohen M. H., Villar-Martin M., 2000, AJ, 120, 562 [4](#), [5](#), [7](#)
- Tueller J., Baumgartner W. H., Markwardt C. B., Skinner G. K., Mushotzky R. F., Ajello M., Barthelmy S., Beardmore A., Brandt W. N., Burrows D., Chincarini G., Campana S., Cummings J., Cusumano G., Evans P., Fenimore E., Gehrels N., Godet O., Grupe D., Holland S., Kennea J., Krimm H. A., Koss M., Moretti A., Mukai K., Osborne J. P., Okajima T., Pagani C., Page K., Palmer D., Parsons A., Schneider D. P., Sakamoto T., Sambruna R., Sato G., Stamatikos M., Strohm M., Ukwata T., Winter L., 2010, ApJS, 186, 378 [6](#)
- Veilleux S., Cecil G., Bland-Hawthorn J., 2005, ARA&A, 43, 769 [2](#)
- Vikhlinin A., Kravtsov A., Forman W., Jones C., Markevitch M., Murray S. S., Van Speybroeck L., 2006, ApJ, 640, 691 [7](#)
- Vikhlinin A., Markevitch M., Murray S. S., Jones C., Forman W., Van Speybroeck L., 2005, ApJ, 628, 655 [4](#)
- Voit G. M., Cavagnolo K. W., Donahue M., Rafferty D. A., McNamara B. R., Nulsen P. E. J., 2008, ApJ, 681, L5 [8](#)
- Volonteri M., Rees M. J., 2005, ApJ, 633, 624 [9](#)
- Waters C. Z., Zepf S. E., 2005, ApJ, 624, 656 [3](#)
- Wise M. W., McNamara B. R., Nulsen P. E. J., Houck J. C., David L. P., 2007, ApJ, 659, 1153 [3](#), [5](#)
- Zdziarski A. A., Lubinski P., Smith D. A., 1999, MNRAS, 303, L11 [6](#)

**Table 1.** SUMMARY OF X-RAY SUBSTRUCTURE SIGNIFICANCE TESTS.

Source (1)	Method-1 (2)	Method-2 (3)
NEx	$1.54 \pm 0.09$	$1.57 \pm 0.12$
EEx	$1.39 \pm 0.05$	$1.56 \pm 0.08$
WEx	$1.47 \pm 0.11$	$1.51 \pm 0.06$
NW Cavity	$0.78 \pm 0.08$	$0.84 \pm 0.04$
SE Cavity	$0.71 \pm 0.10$	$0.76 \pm 0.06$

Details of test methods are given in Section 3. Col. (1) Source region; Col. (2) decrement of structure relative to surface brightness model-B; Col. (3) surface brightness decrement over equal-width annulus.

**Table 2.** SUMMARY OF CAVITY PROPERTIES.

Cavity –	$r$ kpc	$l$ kpc	$t_{\text{sonic}}$ $10^6$ yr	$pV$ $10^{58}$ ergs	$E_{\text{cav}}$ $10^{59}$ ergs	$P_{\text{cav}}$ $10^{44}$ ergs $\text{s}^{-1}$
(1)	(2)	(3)	(4)	(5)	(6)	(7)
NW	6.40	58.3	$50.5 \pm 7.6$	$5.78 \pm 1.07$	$2.31 \pm 0.43$	$1.45 \pm 0.35$
SE	6.81	64.0	$55.4 \pm 8.4$	$6.99 \pm 1.29$	$2.80 \pm 0.52$	$1.60 \pm 0.38$

Col. (1) Cavity location; Col. (2) Radius of excavated cylinder; Col. (3) Length of excavated cylinder; Col. (4) Sound speed age; Col. (5)  $pV$  work; Col. (6) Cavity energy; Col. (7) Cavity power.

**Table 3.** SUMMARY OF X-RAY EXCESSES SPECTRAL FITS.

Region –	$kT_X$ keV	$\eta$ $10^{-5} \text{ cm}^{-5}$	$E_G$ keV	$\sigma_G$ keV	$\eta_G$ $10^{-6} \text{ cm}^{-2} \text{ s}^{-1}$	Cash –	DOF –
(1)	(2)	(3)	(4)	(5)	(6)	(7)	(8)
EEx	$3.03^{+1.19}_{-0.74}$	$5.80^{+1.07}_{-0.97}$	–	–	–	524	430
EEx	$3.68^{+3.34}_{-1.58}$	$2.73^{+0.98}_{-0.94}$	[0.89, 1.42, 4.23]	[0.04, 0.16, 3.6E-4]	[1.2, 2.0, 0.16]	384	430
EEx Bgd	$3.92^{+0.35}_{-0.31}$	$39.9^{+0.18}_{-0.17}$	–	–	–	471	430
WEx	$2.55^{+2.61}_{-0.98}$	$0.66^{+0.11}_{-0.07}$	–	–	–	387	430

Metal abundance was fixed at  $0.5 Z_{\odot}$  for all fits. Col. (1) Extraction region; Col. (2) Thermal gas temperature; Col. (3) Model normalization; Col. (4) Gaussian central energies; Col. (5) Gaussian dispersions; Col. (6) Gaussian normalizations; Col. (7) Modified Cash statistic; Col. (8) Degrees of freedom.

**Table 4.** SUMMARY OF NUCLEAR SOURCE SPECTRAL FITS.

Component (1)	Parameter (2)	SP09 (3)	SP99 (4)
PEXRAV	$\Gamma$	$1.71^{+0.23}_{-0.65}$	fixed to SP09
–	$\eta_P$	$8.07^{+0.64}_{-0.62} \times 10^{-4}$	$8.46^{+2.08}_{-2.12} \times 10^{-4}$
GAUSSIAN 1	$E_G$	$0.73^{+0.05}_{-0.24}$	$0.61^{+0.10}_{-0.05}$
–	$\sigma_G$	$85^{+197}_{-53}$	$97^{+150}_{-97}$
–	$\eta_G$	$8.14^{+3.74}_{-5.82} \times 10^{-6}$	$1.65^{+1.52}_{-1.00} \times 10^{-5}$
GAUSSIAN 2	$E_G$	$1.16^{+0.19}_{-0.33}$	$0.90^{+0.17}_{-0.90}$
–	$\sigma_G$	$383^{+610}_{-166}$	$506^{+314}_{-262}$
–	$\eta_G$	$1.03^{+3.22}_{-0.48} \times 10^{-5}$	$1.48^{+2.68}_{-1.16} \times 10^{-5}$
GAUSSIAN 3	$E_G$	$4.45^{+0.04}_{-0.04}$	$4.46^{+0.04}_{-0.07}$
–	$\sigma_G$	$45^{+60}_{-45}$	$31^{+94}_{-31}$
–	$\eta_G$	$2.67^{+0.91}_{-0.86} \times 10^{-6}$	$6.45^{+4.17}_{-3.69} \times 10^{-6}$
–	$\text{EW}_{K\alpha}^{\text{corr}}$	$531^{+211}_{-218}$	$1210^{+720}_{-710}$
Statistic	$\chi^2$	79.0	7.9
–	DOF	74	15

Fe  $K\alpha$  equivalent widths have been corrected for redshift. Units for parameters:  $\Gamma$  is dimensionless,  $\eta_P$  is in  $\text{ph keV}^{-1} \text{ cm}^{-2} \text{ s}^{-1}$ ,  $E_G$  are in keV,  $\sigma_G$  are in eV,  $\eta_G$  are in  $\text{ph cm}^{-2} \text{ s}^{-1}$ ,  $\text{EW}_{\text{corr}}$  are in eV. Col. (1) XSPEC model name; Col. (2) Model parameters; Col. (3) Values for 2009 CXO spectrum; Col. (4) Values for 1999 CXO spectrum.

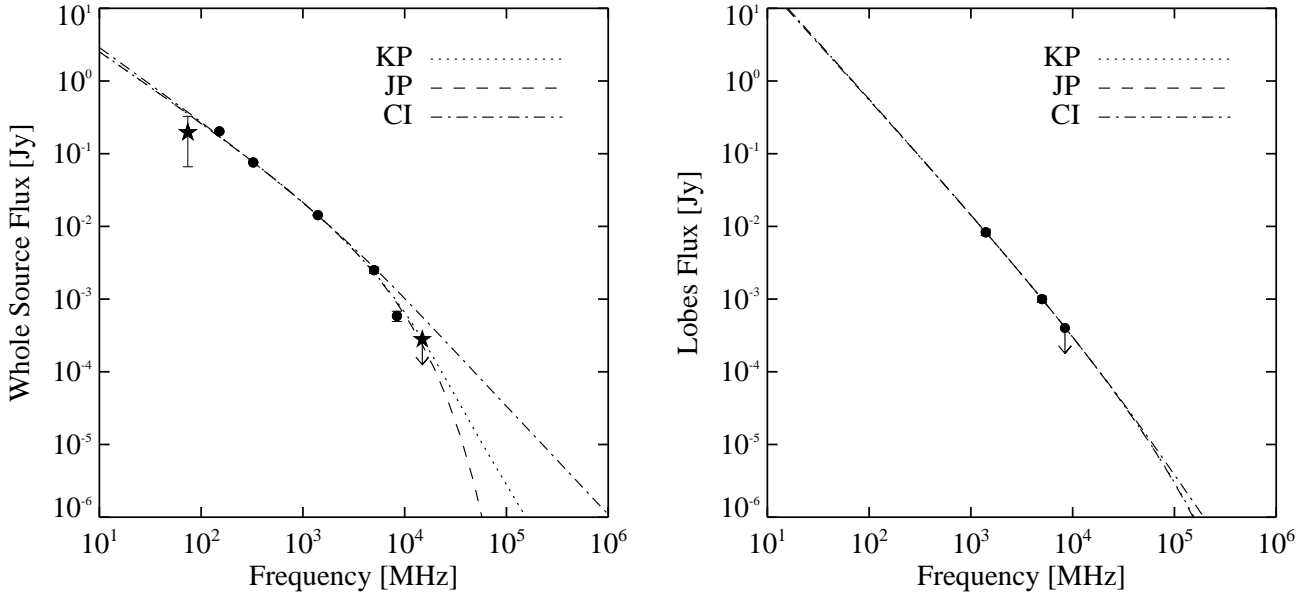


**Figure 1.** Best-fit synchrotron models for the radio spectrum of the full radio source (*left*) and just the lobes (*right*). See Section 2.2 for description of models. Stars denote points excluded in fitting and the upper limits shown are  $1\sigma$ .

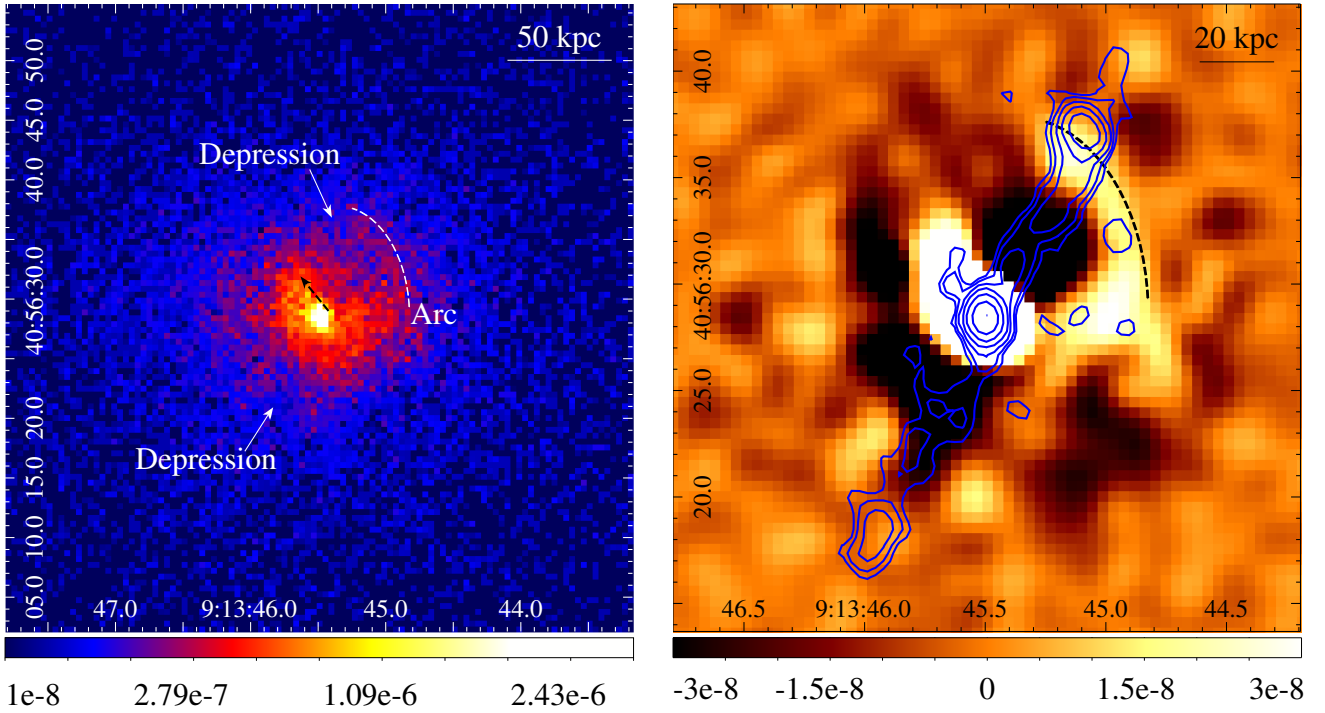


**Figure 2.** CXO 0.5-10.0 keV X-ray clean images of I09. Note the difference in physical area shown in the two panels. *Left:* Box is 300 kpc on a side and the image is unsmoothed. The white dashed curve highlights a faint arc of emission and the dashed black arrow in the nucleus denotes a skewing of core emission toward the NE. Two regions of lower than average surface brightness are also pointed out. *Right:* Unsharp masked image resulting from differencing images smoothed by a  $2''$  and  $5''$  Gaussian. Blue contours are the 1.4 GHz radio emission discussed in Section 2.2, and the dashed black curve is the faint arc from the left panel.



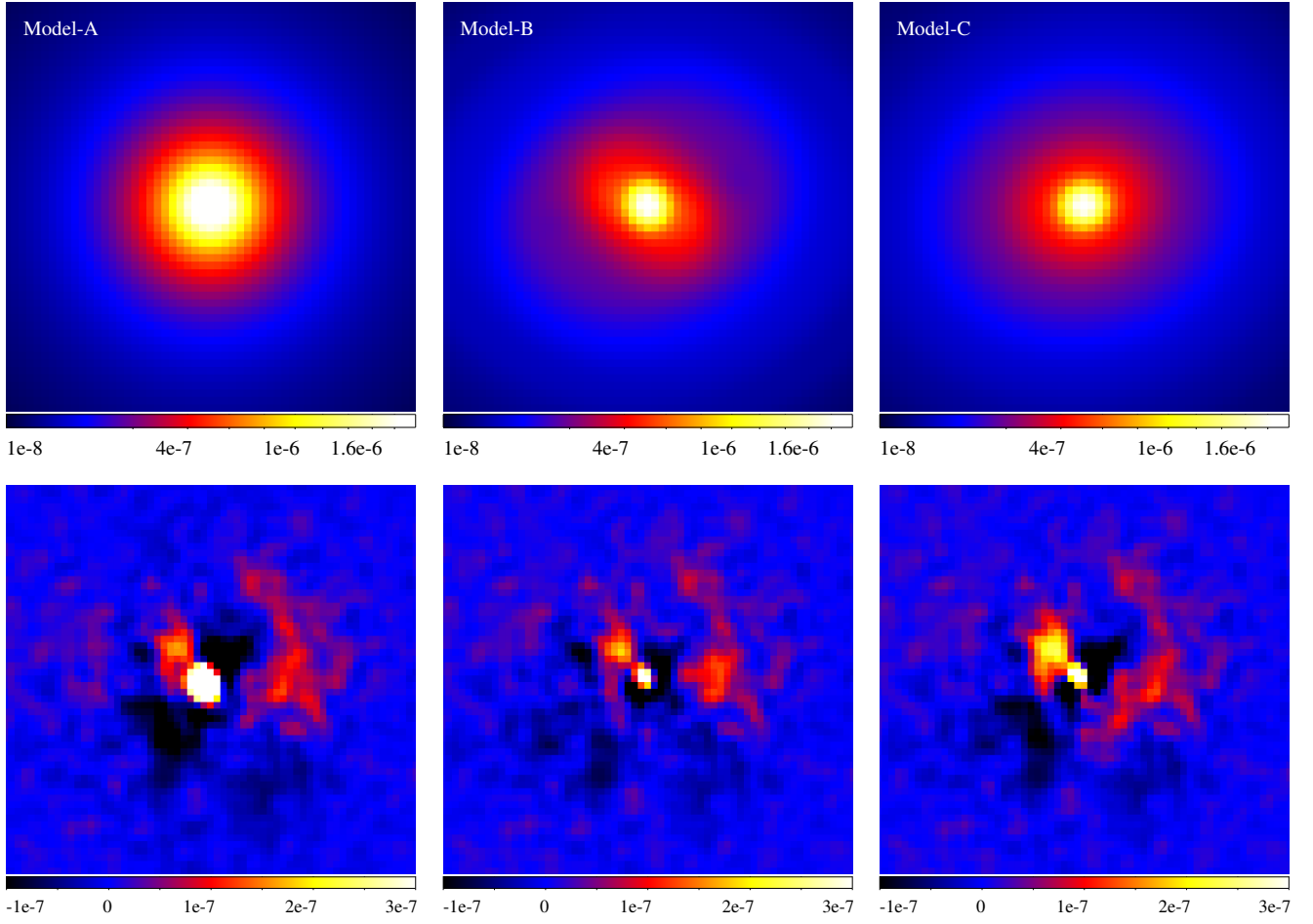


**Figure 3.** Top row are various best-fit surface brightness models (discussed in Section 3), and bottom row are residual images from differencing data and model. All real X-ray images are from the clean *CXO* data, cover the energy range 0.5–7.5 keV, and have units  $\text{ph cm}^{-2} \text{s}^{-1} \text{pix}^{-1}$ . *Left column:* Images using model-A: the double  $\beta$ -model fit to the 1D X-ray surface brightness. *Middle column:* Images using model-B: 2D surface brightness fit with free ellipticity, position angle, and centroid. *Right column:* Images using model-C: 2D surface brightness fit with fixed ellipticity, position angle, and centroid.

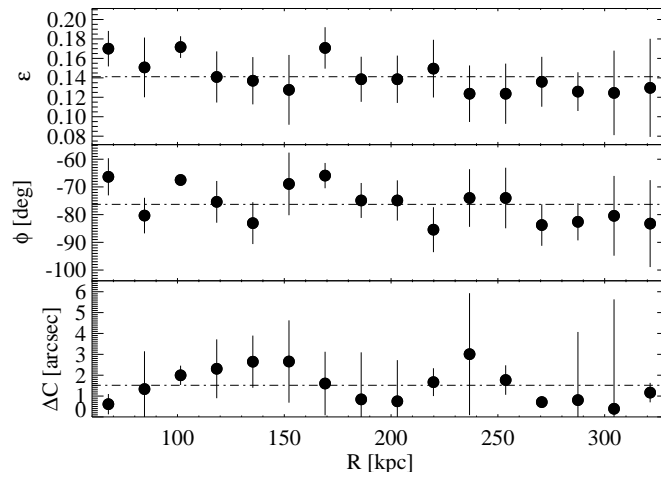


**Figure 4.** Best-fit radial ellipticity ( $\epsilon$ ), position angle ( $\phi$ ), and centroid variation ( $\Delta C$ ) from  $C[\text{J2000}] = (09:13:45.5; +40:56:28.4)$  for 2D X-ray isophotes exterior to the ICM substructures. Mean values are shown as horizontal dashed-dotted lines and have values  $\epsilon = 0.14$ ,  $\phi = -76^\circ$ , and  $\Delta C = 1.5''$ .

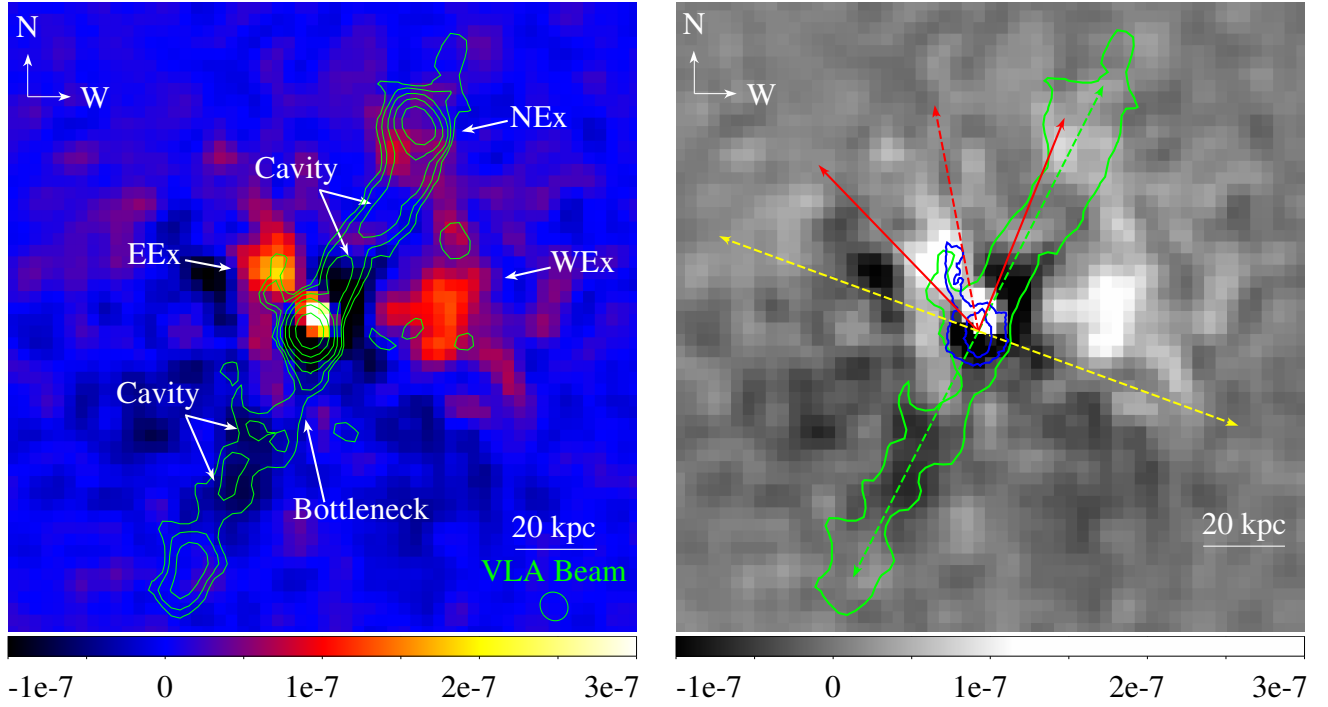


**Figure 5.** *Left:* Residual X-ray image made using surface brightness model-B. Green contours trace 1.4 GHz radio emission above  $3\sigma_{RMS}$ , and regions of interest are labeled. *Right:* Same residual image as left panel with gray-scale biased to lower values. Green contour traces  $3\sigma_{RMS}$  1.4 GHz radio emission, and the dashed green line shows the jet axis. Blue contours trace  $\lambda_{rest} \approx 3900 - 6650 \text{ \AA}$  emission as seen with *HST*. The red dashed and solid lines show the mean direction and opening angle, respectively, of the nuclear UV scattering bicone (see H99 for discussion). Yellow dashed line represents the approximate semi-major axis of the galaxy cluster (see Kleinmann et al. 1988). The EEx lies exactly along the axis of beamed nuclear radiation which is also coincident with the nuclear radio spur.

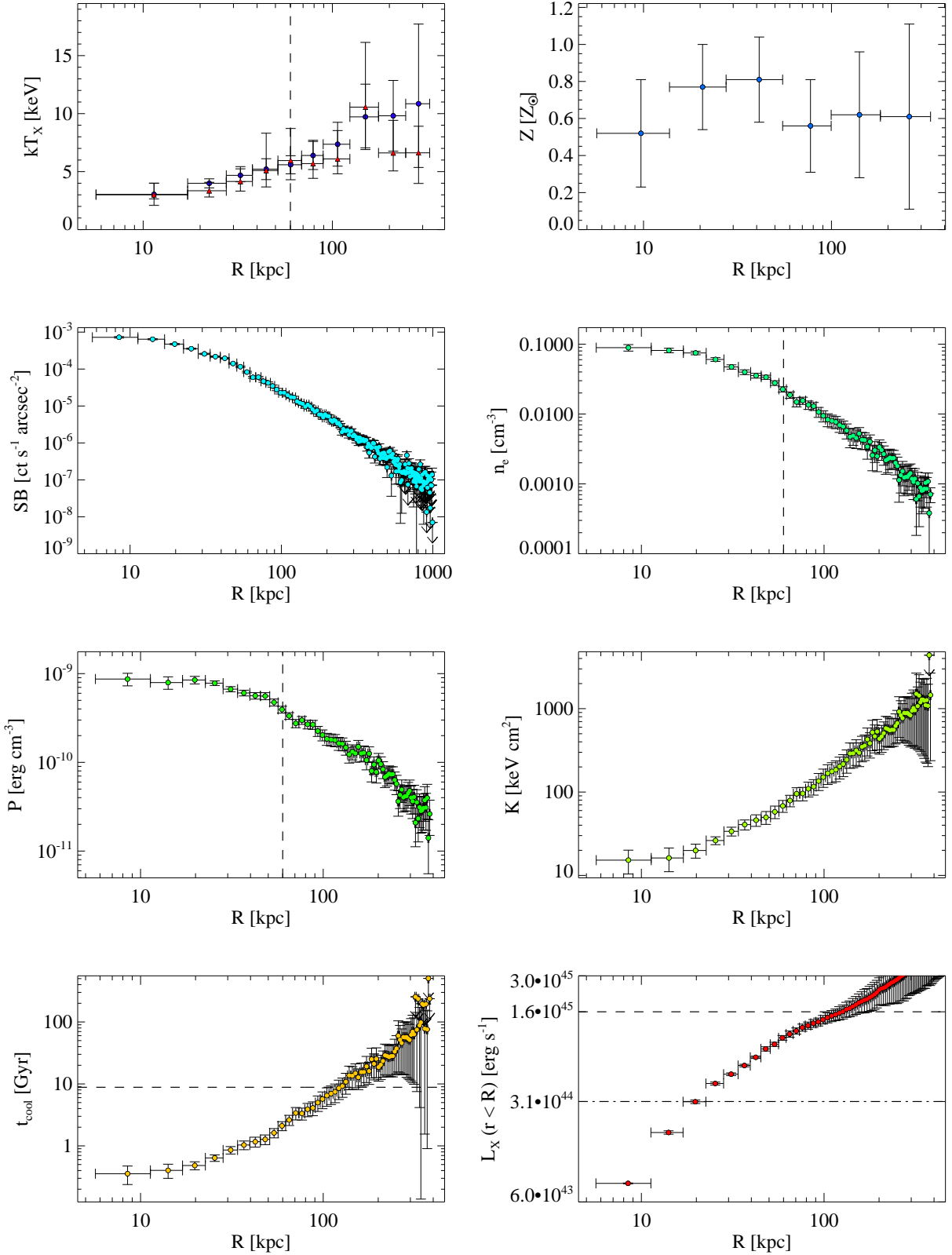


**Figure 6.** Gallery of radial ICM profiles of temperature ( $kT_X$ ), abundance ( $Z$ ), surface brightness ( $SB$ ), gas density ( $n_e$ ), total gas pressure ( $P$ ), entropy ( $K$ ), cooling time ( $t_{cool}$ ), and enclosed X-ray luminosity ( $L_X$ ). Vertical black dashed lines mark the approximate end-points of cavities. Horizontal dashed line in  $t_{cool}$  profile marks  $H_0^{-1}$  at  $z = 0.4418$ . For  $L_X$  profile, dashed line marks  $L_{cool}$ , and dashed-dotted line marks total  $P_{cav}$ .



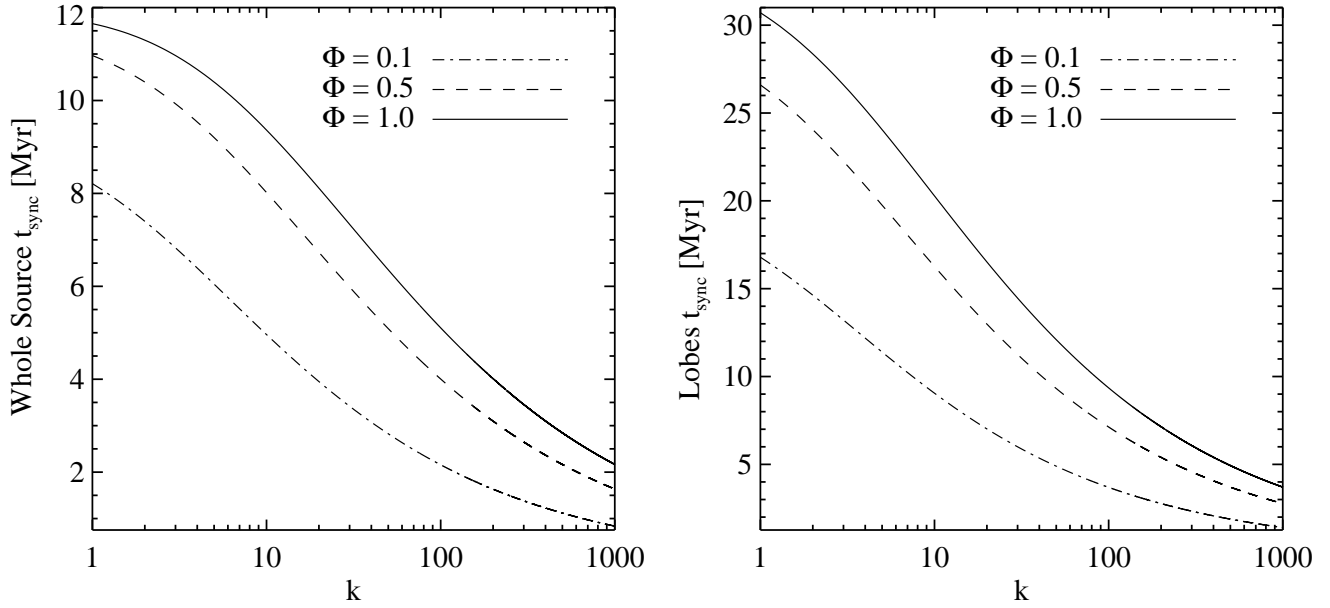


**Figure 7.** Synchrotron age ( $t_{\text{sync}}$ ) as a function of  $k$ , the ratio of lobe energy in non-radiating particles to that in relativistic electrons, for three values of  $\Phi$ , the volume filling factor of the radiating particle population. *Left:* Ages for full radio source; *Right:* ages for lobes only.

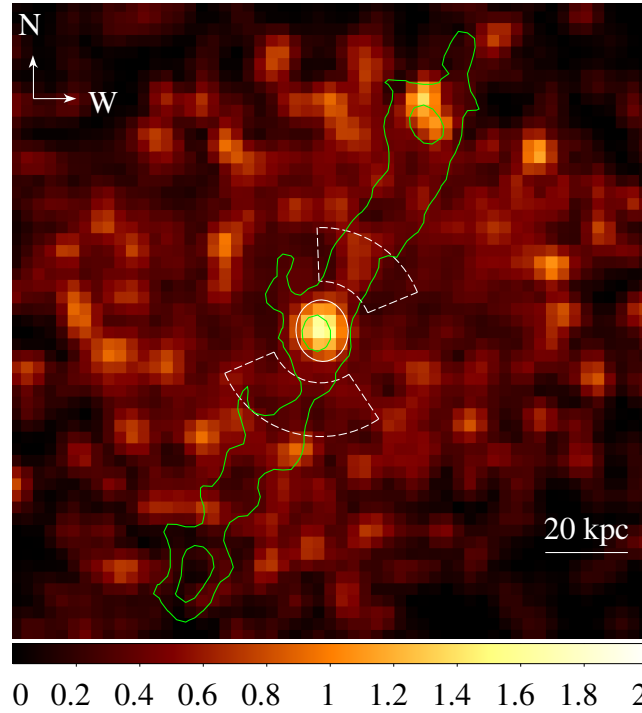


**Figure 8.** Hardness ratio map of I09. Green contours trace the highest and lowest significance regions of the continuous 1.4 GHz radio emission. White ellipse is the 90% EEf source region and dashed white wedges are background regions. The areas with the largest  $HR$  are coincident with the central source and the termination point of the northern radio jet.

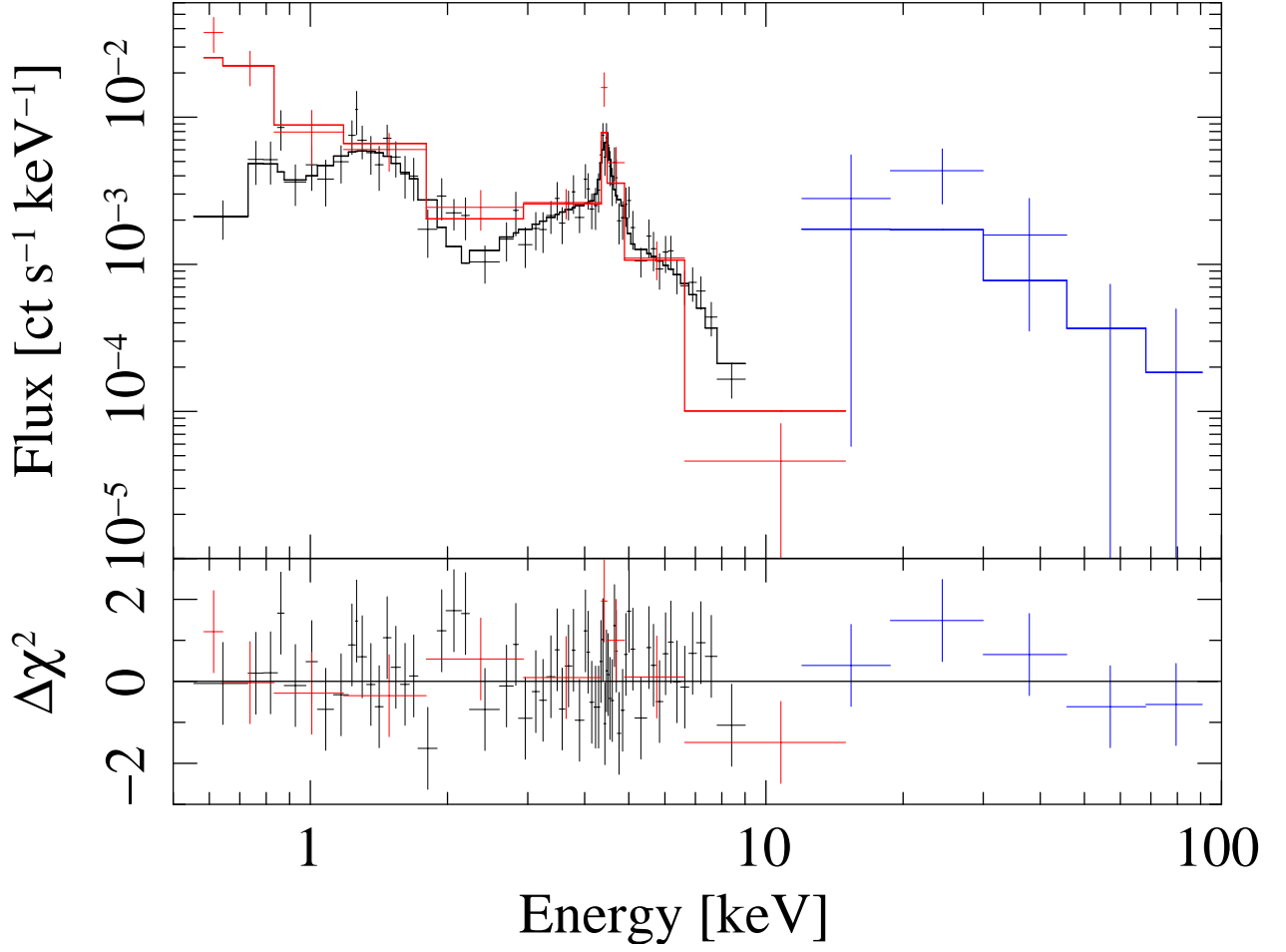


**Figure 9.** Background-subtracted nuclear spectrum and best-fit model for the 1999 (red) & 2009 (black) *CXO* data and 1998 *BeppoSAX* PDS data (blue). Data has been binned to  $3\sigma$  significance. The significant flux difference below 1.3 keV is a result of the greater effective area of the ACIS-S3 CCD in 1999 versus ACIS-I3 in 2009.

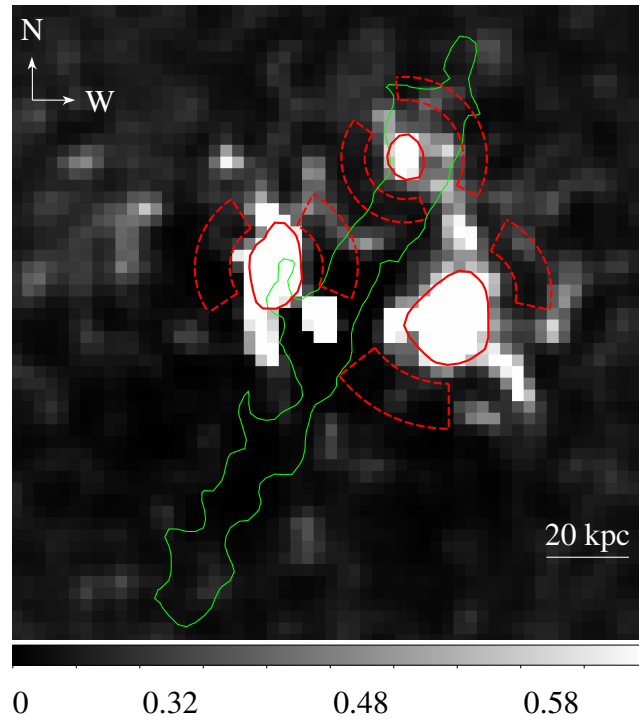


**Figure 10.** Residual X-ray image using model-B after dividing by  $10^{-7}$  and scaling each pixel by a power of 1000 to enhance substructure contrast. The outermost contour of continuous 1.4 GHz radio emission is overlaid for reference. Solid red lines bound spectral extraction regions for each excess, and nearest red dashed wedges bound associated background regions.



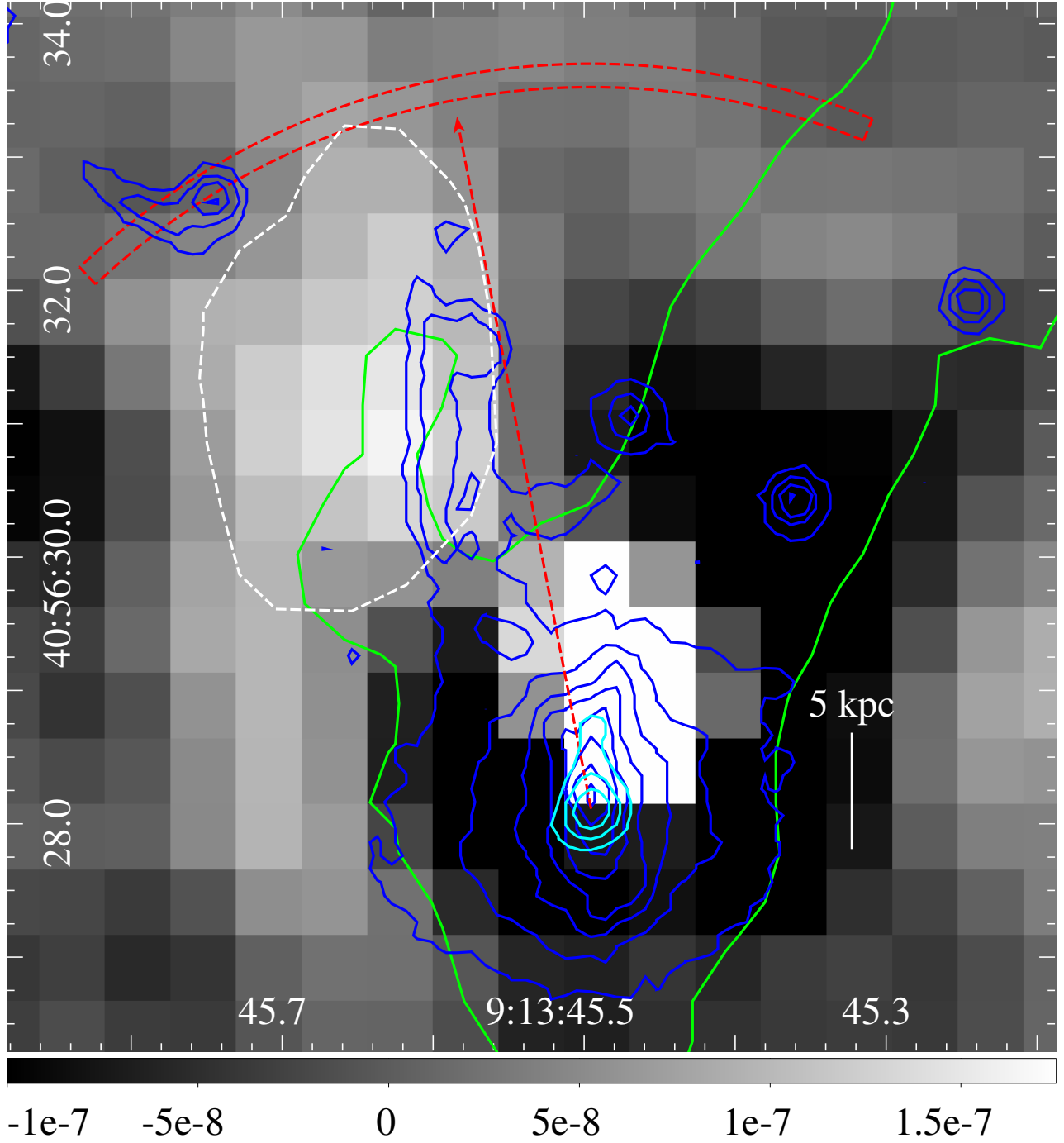


**Figure 11.** Exposure-corrected 0.5–7.5 keV X-ray residual image zoomed-in on the EEx with units  $\text{ph cm}^{-2} \text{s}^{-1} \text{pix}^{-1}$ . Green contour is 1.4 GHz radio emission at  $3\sigma_{\text{rms}}$ , blue contours are optical emission ( $\lambda_{\text{rest}} \approx 3900 - 6650 \text{ \AA}$ ) in 10 log-space steps from  $0.5-50 \text{ ct s}^{-1}$ , and cyan contours are 4.8 GHz radio emission beginning at  $3\sigma_{\text{rms}}$ . The optical plume-like structure to the northeast of the galaxy is a bright [O III] emission nebula (see Crawford & Vnderriest 1996). The red vector denotes the best-fit emission axis for the UV scattering bi-cone, and the red wedge marks its extent and spans the  $3\sigma$  opening angle (see H99). The dashed, white region is the EEx spectral extraction region, note that it was defined without considering the location of any other emission features. The residual nuclear X-ray emission extends exclusively to the north of the nucleus and is where nearly all of the Fe K $\alpha$  emission originates.

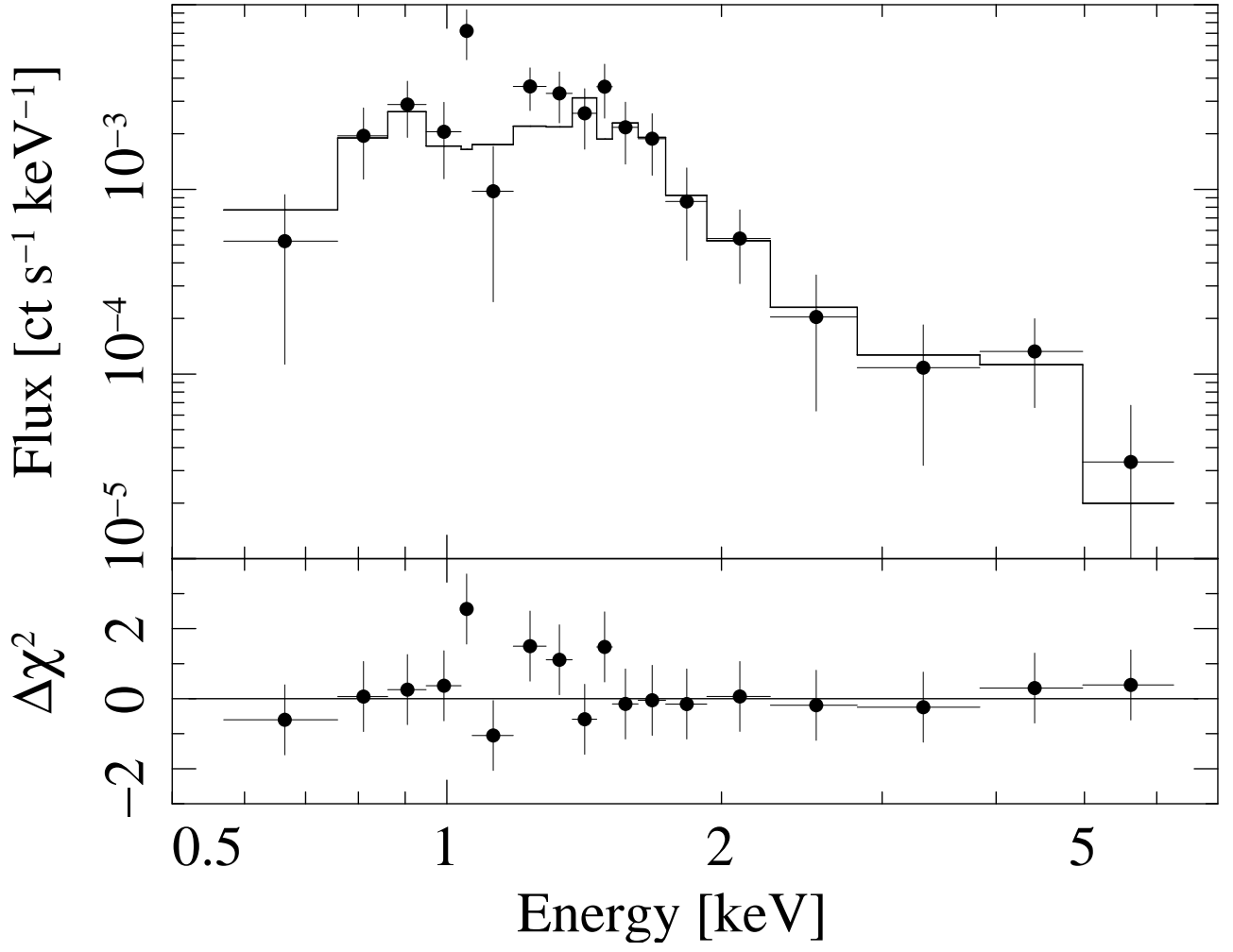


**Figure 12.** Background-subtracted EEx spectrum binned to  $3\sigma$  significance. The black points are data and the solid black line is the normalized CLOUDY model for a quasar irradiated nebula and ICM.

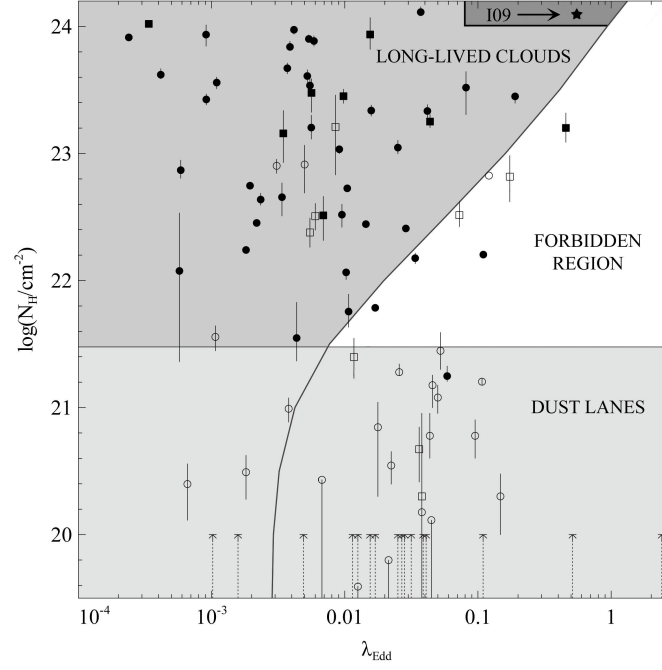


**Figure 13.** Figure taken from [Fabian et al. \(2009\)](#) showing absorbing column density versus the effective Eddington ratio of AGN in the 9-month *Swift*/BAT survey. The general location of I09 is denoted with a star and dark shaded region in the upper right. See [Fabian et al. \(2009\)](#) for details regarding symbols and derivation of various regions where long-lived obscuring clouds exist, dusty clouds experience a super-Eddington AGN, and extended dust lanes form. The curved line denotes  $\lambda_{\text{Edd}}$  for Galactic dust grain abundance.

